*J. Fluid Mech.* (2007), *vol.* 576, *pp.* 109–137.  
doi:10.1017/S002211200600454X Printed in the United Kingdom

# Mean flow of turbulent–laminar patterns in plane Couette flow

DWIGHT BARKLEY[1] AND LAURETTE S. TUCKERMAN[2]

[1]Mathematics Institute, University of Warwick, Coventry, CV4 7AL, UK
barkley@maths.warwick.ac.uk

[2]LIMSI-CNRS, BP 133, 91403 Orsay, France
laurette@limsi.fr

(Received 6 July 2006 and in revised form 13 November 2006)

A turbulent–laminar banded pattern in plane Couette flow is studied numerically. This pattern is statistically steady, is oriented obliquely to the streamwise direction, and has a very large wavelength relative to the gap. The mean flow, averaged in time and in the homogeneous direction, is analysed. The flow in the quasi-laminar region is not the linear Couette profile, but results from a non-trivial balance between advection and diffusion. This force balance yields a first approximation to the relationship between the Reynolds number, angle, and wavelength of the pattern. Remarkably, the variation of the mean flow along the pattern wavevector is found to be almost exactly harmonic: the flow can be represented via only three cross-channel profiles as $\boldsymbol{U}(x, y, z) \approx \boldsymbol{U}_0(y) + \boldsymbol{U}_c(y)\cos(kz) + \boldsymbol{U}_s(y)\sin(kz)$. A model is formulated which relates the cross-channel profiles of the mean flow and of the Reynolds stress. Regimes computed for a full range of angle and Reynolds number in a tilted rectangular periodic computational domain are presented. Observations of regular turbulent–laminar patterns in other shear flows – Taylor–Couette, rotor–stator, and plane Poiseuille – are compared.

## 1. Introduction

Pattern formation is associated with the spontaneous breaking of spatial symmetry. Many of the most famous and well-studied examples of pattern formation come from fluid dynamics. Among these are the convection rolls which spontaneously form in a uniform layer of fluid heated from below and the Taylor cells which form between concentric rotating cylinders. In these cases continuous translational symmetries are broken by the cellular flows beyond critical values of the control parameter – the Rayleigh number or Taylor number.

A fundamentally new type of pattern has been discovered in large aspect-ratio shear flows in recent years by researchers at GIT-Saclay (Prigent & Dauchot 2000; Prigent *et al.* 2002; Prigent *et al.* 2003; Prigent & Dauchot 2005; Bottin *et al.* 1998). Figure 1 shows an example from plane Couette experiments performed by these researchers. One sees a remarkable spatially periodic pattern composed of distinct regions of turbulent and laminar flow. The pattern itself is essentially stationary. The pattern wavelength is large compared with the gap between the plates and its wavevector is oriented obliquely to the streamwise direction.

The pattern emerges spontaneously from featureless turbulence as the Reynolds number is decreased. This is illustrated in figure 2 with time series from our numerical simulations of plane Couette flow for decreasing Reynolds number (conventionally

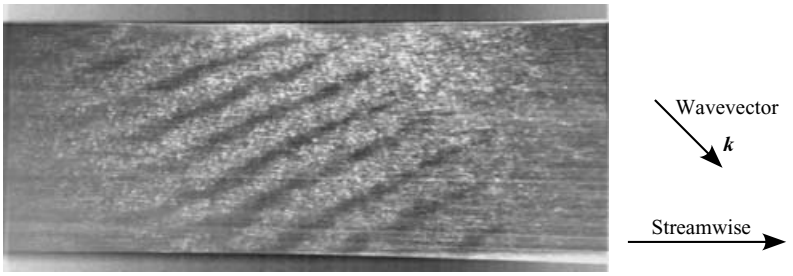


FIGURE 1. Photograph of a turbulent–laminar pattern in plane Couette flow from the Saclay experiment. Light regions correspond to turbulent flow and dark regions to laminar flow. The striped pattern of alternating laminar and turbulent flow forms with a wavevector $\boldsymbol{k}$ oblique to the streamwise direction. The wavelength is approximately 40 times the half-gap between the moving walls. The lateral dimensions are 770 by 340 half-gaps and the Reynolds number is $Re = 385$. Figure reproduced with permission from Prigent *et al.*

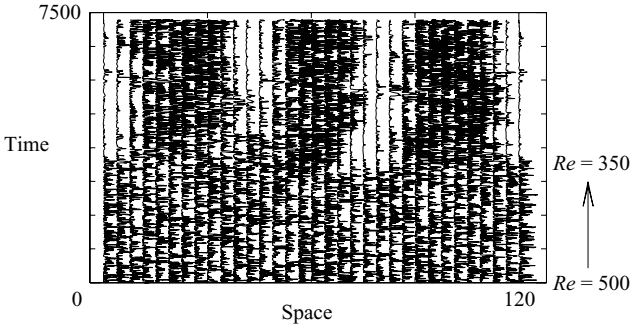


FIGURE 2. Space–time plot from numerical simulations of plane Couette flow showing the spontaneous formation of a turbulent–laminar pattern at $Re = 350$. The kinetic energy in the mid-plane is sampled at 32 equally spaced points along an oblique cut (in the direction of pattern wavevector) through three wavelengths of the pattern. At time zero, $Re = 500$ and the flow is uniformly turbulent. Over about 3000 time units $Re$ is decreased in steps to 350, and then held constant.

defined based on half the velocity difference between the plates and half the gap). At Reynolds number 500, the flow is uniformly turbulent. Following a decrease in the Reynolds number below 400 (specifically 350 in figure 2) the flow organizes into three regions of relatively laminar flow and three regions of more strongly turbulent flow. While the fluid in the turbulent regions is very dynamic, the pattern is essentially steady.

Shear flows exhibiting regular coexisting turbulent and laminar regions have been known for many years. In the mid 1960s, a state known as spiral turbulence was discovered (Coles 1965; Van Atta 1966; Coles & Van Atta 1966) in counter-rotating Taylor–Couette flow. Consisting of a turbulent and a laminar region, each with a spiral shape, spiral turbulence was further studied in the 1980s (Andereck, Liu & Swinney 1986; Hegseth *et al.* 1989). Experiments by the Saclay researchers (Prigent & Dauchot 2000; Prigent *et al.* 2002, 2003; Prigent & Dauchot 2005) in a very large aspect-ratio Taylor–Couette system have shown that the turbulent and laminar regions in fact form a periodic pattern, of which the original observations of Coles and Van Atta comprised only one wavelength. Analogues of these states occur in other shear flows as well. Cros & Le Gal (2002) discovered large-scale turbulent spirals in the shear flow

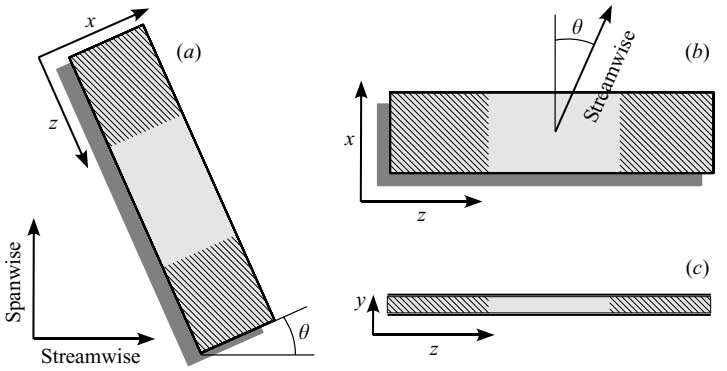


FIGURE 3. Computational domain oriented at angle $\theta$ to the streamwise–spanwise directions. The $z$-direction is aligned to the pattern wavevector while the $x$-direction is perpendicular to the pattern wavevector. The turbulent region is represented schematically by hatching. (*a*) Domain oriented with streamwise velocity horizontal, as in figure 1. (*b*) Domain oriented with $z$ horizontal, as it will be represented in this paper. In (*a*), (*b*) the near (upper) plate moves in the streamwise direction; the far (lower) plate in the opposite direction. (*c*) View between the plates.

between a stationary and a rotating disk. Tsukahara *et al.* (2005) observed oblique turbulent–laminar bands in plane Poiseuille flow. A unified Reynolds number based on the shear and the half-gap can be defined for these different flows (Prigent *et al.* 2003) and is described in the Appendix. When converted to comparable quantities in this way, the Reynolds-number thresholds, wavelengths, and angles are similar for all of these turbulent patterned flows. The patterns are always found near the minimum Reynolds numbers for which turbulence can exist in the flow.

In this paper we present a detailed analysis of these turbulent–laminar patterns. We will focus on a single case – the periodic pattern at Reynolds number 350. From computer simulations, we obtain the flow and identify the symmetries of the patterned state. We consider in detail the force balance responsible for maintaining the pattern. From the symmetries and harmonic content we are able to reduce the description to six ordinary differential equations which very accurately describe the patterned mean flow.

## 2. Preliminaries

### 2.1. *Geometry*

The unusual but key feature of our study of turbulent–laminar patterns is the use of simulation domains aligned with the pattern wavevector and thus tilted relative to the streamwise–spanwise directions of the flow. Figure 3 illustrates this and defines our coordinate system. In figure 3(*a*) a simulation domain is shown as it would appear relative to an experiment, figure 1, in which the streamwise direction (defined by the direction of plate motion) is horizontal. The near (upper) plate moves to the right and the far (lower) plate to the left in the figure. As we have discussed in detail (Barkley & Tuckerman 2005*a*, *b*), simulating the flow in a tilted geometry has advantages in reducing computational expense and in facilitating the study of pattern orientation and wavelength selection. The important point for the present study is that the coordinates are aligned to the patterns. The $z$-direction is parallel to the pattern wavevector while the $x$-direction is perpendicular to the wavevector (compare figure 3(*a*) with figure 1).

Figures 3(*b*) and 3(*c*) show the simulation domain as it will be oriented in this paper. In this orientation the streamwise direction is tilted at angle $\theta$ (here 24°) to the $x$-direction. This choice of angle is guided by the experimental results and by our previous simulations. (In past publications (Barkley & Tuckerman 2005*a*, *b*) we have used un-primed $x, z$ coordinates for those aligned along spanwise-streamwise directions and primes for coordinates tilted with the simulation domain. Here we focus exclusively on coordinates fixed to the simulation domain and so for convenience denote them without primes.) In these tilted coordinates, the streamwise direction is

$$\boldsymbol{e}_x \cos\theta + \boldsymbol{e}_z \sin\theta \equiv \alpha \boldsymbol{e}_x + \beta \boldsymbol{e}_z, \tag{2.1}$$

where

$$\alpha \equiv \cos\theta = \cos(24^\circ) = 0.913, \qquad \beta \equiv \sin\theta = \sin(24^\circ) = 0.407. \tag{2.2}$$

We take $L_x = 10$, for the reasons explained in Jiménez & Moin (1991), Hamilton, Kim & Waleffe (1995), Waleffe (2003) and Barkley & Tuckerman (2005*a*, *b*). Essentially, $L_x \sin\theta$ must be near 4 in order to contain one pair of streaks or spanwise vortices, which are necessary to the maintenance of low-Reynolds-number wall-bounded turbulence. Although our simulations are in a three-dimensional domain, we will average the results in the homogeneous $x$ direction, as will be explained in § 2.3. For most purposes it is sufficient to view the flow in the $z, y$ coordinates illustrated in figure 3(*c*). The mid-plane between the plates corresponds to $y = 0$.

The length $L_z$ of our computational domain is guided by the experimental results and by our previous simulations. One of the distinctive features of the turbulent–laminar patterns is their long wavelength relative to the gap between the plates. A standard choice for length units in plane Couette flow is the half-gap between the plates. In the simulation with $L_z = 120$ and $\theta = 24^\circ$ shown in figure 2, a pattern of wavelength 40 emerged spontaneously from uniform turbulence when the Reynolds number was lowered to $Re = 350$. For this reason, the simulations we will describe below are conducted with $L_z = \lambda_z = 40$. The corresponding wavenumber is

$$k \equiv \frac{2\pi}{40} = 0.157. \tag{2.3}$$

This large wavelength, or small wavenumber, expresses the fact that the pattern wavelength in $z$ is far greater than the cross-channel dimension.

### 2.2. *Equations and numerics*

The flow is governed by the incompressible Navier–Stokes equations

$$\frac{\partial \boldsymbol{u}}{\partial t} = -(\boldsymbol{u}\cdot\nabla)\boldsymbol{u} - \nabla p + \frac{1}{Re}\nabla^2 \boldsymbol{u} \quad \text{in } \Omega, \tag{2.4a}$$

$$0 = \nabla \cdot \boldsymbol{u} \quad \text{in } \Omega, \tag{2.4b}$$

where $\boldsymbol{u}(\boldsymbol{x}, t)$ is the velocity field and $p(\boldsymbol{x}, t)$ is the static pressure. Without loss of generality the density is taken to be one. The equations have been non-dimensionalized by the plate speed and the half-gap between the plates. $\Omega$ is the tilted computational domain discussed in the previous section.

No-slip boundary conditions are imposed at the plates and periodic boundary conditions are imposed in the lateral directions. In our coordinates the conditions are

$$\boldsymbol{u}(x, y = \pm 1, z) = \pm(\boldsymbol{e}_x \cos\theta + \boldsymbol{e}_z \sin\theta), \tag{2.5a}$$

$$\boldsymbol{u}(x + L_x, y, z) = \boldsymbol{u}(x, y, z), \tag{2.5b}$$

$$\boldsymbol{u}(x, y, z + L_z) = \boldsymbol{u}(x, y, z). \tag{2.5c}$$

Linear Couette flow $\boldsymbol{u}^L$ is a solution to (2.4)–(2.5), which is stable for all $Re$ and satisfies

$$\nabla^2 \boldsymbol{u}^L = (\boldsymbol{u}^L \cdot \nabla)\boldsymbol{u}^L = 0. \tag{2.6}$$

In our tilted coordinate system,

$$\boldsymbol{u}^L = y(\boldsymbol{e}_x \cos\theta + \boldsymbol{e}_z \sin\theta) = y(\alpha \boldsymbol{e}_x + \beta \boldsymbol{e}_z) = u^L \boldsymbol{e}_x + w^L \boldsymbol{e}_z. \tag{2.7}$$

The Navier–Stokes equations (2.4) with boundary conditions (2.5) are simulated using the spectral element ($x$–$y$)-Fourier ($z$) code `Prism` (Henderson & Karniadakis 1995). We use a spatial resolution consistent with previous studies (Hamilton *et al.* 1995; Waleffe 2003). Specifically, for a domain with dimensions $L_x = 10$ and $L_y = 2$, we use a computational grid with 10 elements in the $x$-direction and 5 elements in the $y$-direction. Within each element, we use eighth-order polynomial expansions for the primitive variables. In the $z$-direction, a Fourier representation is used and the code is parallelized over the Fourier modes. Our domain with $L_z = 40$ is discretized with 512 Fourier modes or gridpoints. Thus the total spatial resolution we use for the $L_x \times L_y \times L_z = 10 \times 2 \times 40$ domain can be expressed as $N_x \times N_y \times N_z = 81 \times 41 \times 512 = 1.7 \times 10^6$ modes or gridpoints.

### 2.3. *Dataset and averaging*

The focus of this paper is the mean field calculated from the simulation illustrated by the spatio-temporal diagram in figure 4(*a*). The velocity field in the portion of the domain shows high-frequency and high-amplitude fluctuations, while the flow in the right portion is basically quiescent. We will call the flow on the left turbulent, even though it could be argued that it is not fully developed turbulence. We will call the flow on the right laminar, even though occasional small fluctuations can be seen in this region.

The turbulent–laminar pattern persists during the entire simulation of $14 \times 10^3$ time units. However the pattern undergoes short-scale 'jiggling', seen particularly at the edges of the turbulent regions, and longer-scale drifting or wandering in the periodic $z$-direction. We seek to describe the field which results from smoothing the turbulent fluctuations, but for which drifting is minimal, by averaging over an appropriate time interval. The desired averaging time interval represents a compromise between the short and long time scales. We have chosen to average the flow in figure 4(*a*) over the shaded time interval $[t, t+T] = [6000, 8000]$, during which the pattern is approximately stationary.

The time-averaged flow is homogeneous in the $x$-direction. This is illustrated in figure 4(*b*) where we plot one of the velocity components time-averaged flow over the interval [6000, 8000]. Cuts at different $x$ locations show that there is essentially no variation in the $x$-direction. All other quantities are similarly independent of $x$. It is therefore appropriate to consider mean flows as averages over the $x$-direction as well as over the time.

We define mean flows as

$$\langle \boldsymbol{u} \rangle(y, z) \equiv \frac{1}{T}\frac{1}{L_x}\int_t^{t+T}\int_0^{L_x} \boldsymbol{u}(x, y, z, t)\,\mathrm{d}x\,\mathrm{d}t, \tag{2.8a}$$

$$\langle p \rangle(y, z) \equiv \frac{1}{T}\frac{1}{L_x}\int_t^{t+T}\int_0^{L_x} p(x, y, z, t)\,\mathrm{d}x\,\mathrm{d}t. \tag{2.8b}$$

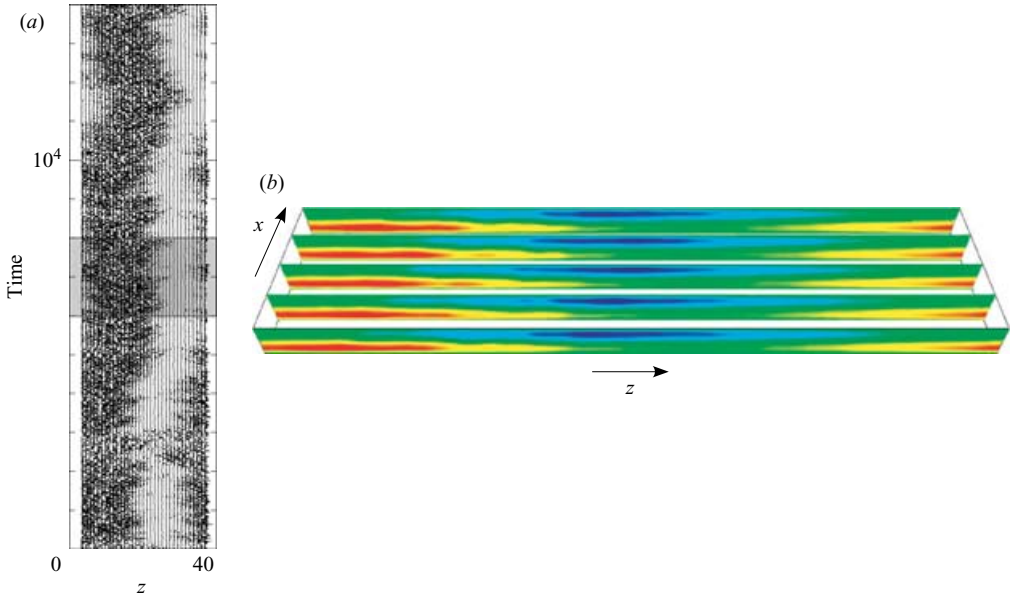


FIGURE 4. (*a*) Time series of a turbulent–laminar pattern. The kinetic energy $E = \boldsymbol{u}\cdot\boldsymbol{u}/2$ is shown along the line $x = y = 0$ at 32 equally spaced points in $z$ for $0 \leqslant t \leqslant 14000$. The interval [6000, 8000] used for time averaging is shown in grey. (*b*) Time-averaged velocity at five $x$-locations illustrating the $x$-independence of the time-averaged flow. We have plotted $\frac{1}{T}\int \mathrm{d}t(u - u^L)$, the average $x$-component of velocity with linear Couette flow subtracted, averaged over the interval [6000, 8000] indicated in (*a*). Colour range from blue to red: [–0.4, 0.4].

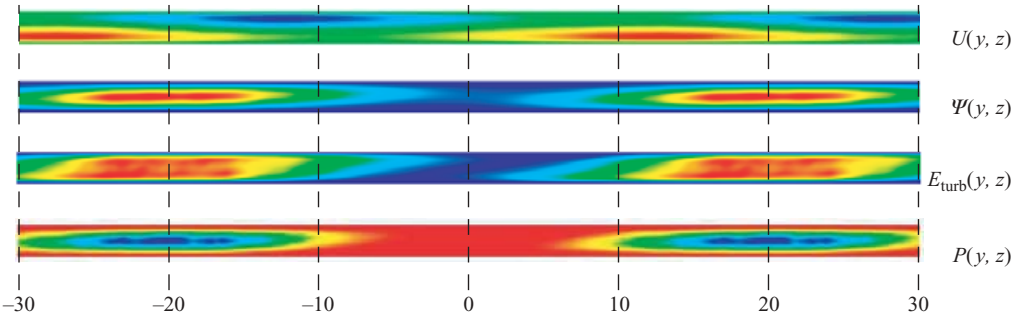


FIGURE 5. $U(y, z)$: transverse component of mean flow. $\Psi(y, z)$: streamfunction of in-plane mean flow. A long cell extends from one laminar–turbulent boundary to the other. Gradients of $\Psi$ are much larger in $y$ than in $z$, i.e. $|W| \gg |V|$. In the laminar region at the centre, $W, V \approx 0$. $E_{\mathrm{turb}}(y, z)$: mean turbulent kinetic energy $\langle \tilde{\boldsymbol{u}}\cdot\tilde{\boldsymbol{u}}\rangle/2$. There is a phase difference of $\lambda_z/4 = 10$ between extrema of $E_{\mathrm{turb}}$ and of $U$. $P(y, z)$: mean pressure field. Pressure gradients are primarily in the $y$-direction and within the turbulent region. Colour ranges for each field from blue to red: $U$ [–0.4, 0.4], $\Psi$ [0, 0.09], $E_{\mathrm{turb}}$ [0, 0.4], P [0, 0.007].

The mean fields obey the averaged Navier–Stokes equations

$$0 = -(\langle \boldsymbol{u}\rangle\cdot\nabla)\langle \boldsymbol{u}\rangle - \langle(\tilde{\boldsymbol{u}}\cdot\nabla)\tilde{\boldsymbol{u}}\rangle - \nabla\langle p\rangle + \frac{1}{Re}\nabla^2\langle \boldsymbol{u}\rangle, \tag{2.9a}$$

$$0 = \nabla\cdot\langle \boldsymbol{u}\rangle, \tag{2.9b}$$

where

$$\tilde{\boldsymbol{u}} \equiv \boldsymbol{u} - \langle \boldsymbol{u}\rangle \tag{2.10}$$

is the fluctuating field and $\langle\rangle$ denotes the $x$–$t$ average. The mean fields are subject to the same boundary conditions as equations (2.4). We denote the Reynolds-stress force from the fluctuating field in equations (2.9) by $\boldsymbol{F}$:

$$\boldsymbol{F} \equiv -\langle(\tilde{\boldsymbol{u}}\cdot\nabla)\,\tilde{\boldsymbol{u}}\rangle = -\nabla\cdot\langle\tilde{\boldsymbol{u}}\tilde{\boldsymbol{u}}\rangle, \tag{2.11}$$

We shall focus almost exclusively on the difference between the mean flow and linear Couette flow, for which we introduce the notation

$$\boldsymbol{U} \equiv \langle\boldsymbol{u}\rangle - \boldsymbol{u}^L, \tag{2.12}$$

as well as $P \equiv \langle p\rangle$.

Letting the components of $\boldsymbol{U}$ be denoted by $(U, V, W)$ and the components of $\boldsymbol{F}$ be denoted by $(F^U, F^V, F^W)$, then the averaged Navier–Stokes equations for the deviation from linear Couette flow in component form become

$$0 = -(V\partial_y + (W+\beta y)\partial_z)(U+\alpha y) + \frac{1}{Re}\left(\partial_y^2+\partial_z^2\right)U + F^U \tag{2.13a}$$

$$0 = -(V\partial_y + (W+\beta y)\partial_z)V - \partial_y P + \frac{1}{Re}\left(\partial_y^2+\partial_z^2\right)V + F^V \tag{2.13b}$$

$$0 = -(V\partial_y + (W+\beta y)\partial_z)(W+\beta y) - \partial_z P + \frac{1}{Re}\left(\partial_y^2+\partial_z^2\right)W + F^W \tag{2.13c}$$

$$0 = \partial_y V + \partial_z W. \tag{2.13d}$$

$\boldsymbol{U}$ is required to satisfy homogeneous boundary conditions at the plates

$$\boldsymbol{U}(y=\pm 1, z) = \boldsymbol{0} \tag{2.14}$$

and periodic boundary conditions in $z$.

A system of this type, with three components depending on two coordinates, is sometimes called 2.5 dimensional. The transverse, or out-of-plane flow $U(y,z)$ appears only in the first equation and is effectively a passive scalar advected by the in-plane flow $(V, W)$ and driven by the Reynolds-stress force $F^U$. The in-plane flow can be expressed in terms of a streamfunction $\Psi$ where

$$V\boldsymbol{e}_y + W\boldsymbol{e}_z = \boldsymbol{e}_x\times\nabla\Psi = -\partial_z\Psi\boldsymbol{e}_y + \partial_y\Psi\boldsymbol{e}_z. \tag{2.15}$$

We shall use both $(U, V, W)(y,z)$ and $(U,\Psi)(y,z)$ to describe the mean flows.

## 3. Results

We present a characterization of the turbulent–laminar pattern at $Re = 350$. We describe in detail the mean flow, its symmetries, and the dominant force balances within the flow. Our goal here is not to consider closures for averaged Navier–Stokes equations (2.13). We will make no attempt to model the turbulence, i.e. to relate the Reynolds-stress tensor $\langle\tilde{\boldsymbol{u}}\tilde{\boldsymbol{u}}\rangle$ to the mean flow $\boldsymbol{U}$. Instead we use fully resolved (three-dimensional, time-dependent) numerical simulations of the turbulent flow to measure both the mean field $\boldsymbol{U}$ and Reynolds-stress force $\boldsymbol{F}$. From these we extract the structure of these fields and the dominant force balances at play in sustaining turbulent–laminar patterns.

### 3.1. *Mean flow*

The mean flow is visualized in figure 5 via the transverse, out-of-plane flow $U(y,z)$ and the in-plane streamfunction $\Psi(y,z)$. Recall (equation (2.12)) that these fields are

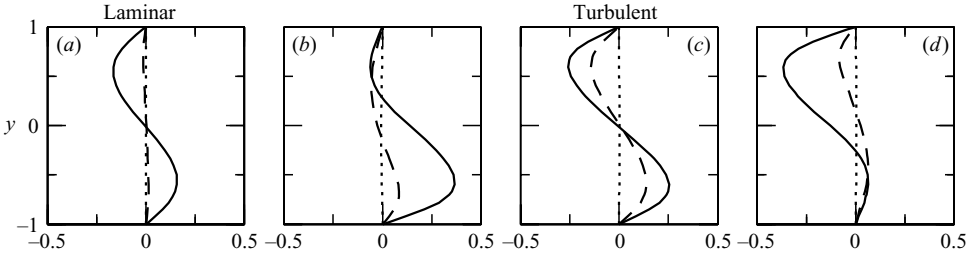


FIGURE 6. Mean flow profiles in $y$ at four equally spaced locations in $z$. ($a$) Centre of the laminar region ($z=0$), ($b$) laminar–turbulent boundary ($z=10$), ($c$) centre of the turbulent region ($z=20$) and ($d$) turbulent–laminar boundary ($z=-10$). Components $U$ (solid), $V$ (dotted), $W$ (dashed) of deviation from linear Couette flow $\boldsymbol{u}^L$. In the laminar region, $W\approx 0$, indicating no deviation from $u^L$. $V$ is very small throughout.

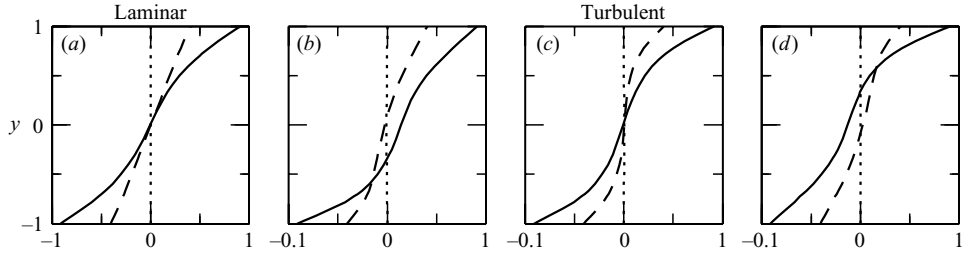


FIGURE 7. The same as in figure 6, but with laminar Couette flow $\boldsymbol{u}^L$ included.

the deviations of the mean flow from linear Couette flow $\boldsymbol{u}^L$. The mean turbulent kinetic energy

$$E_{\mathrm{turb}} \equiv \tfrac{1}{2}\langle \tilde{\boldsymbol{u}}\cdot\tilde{\boldsymbol{u}}\rangle \tag{3.1}$$

serves to clearly identify the turbulent region. In these and subsequent plots, the middle of the laminar region is positioned at the centre of the figure and the turbulent region at the periodic boundaries of the computational domain. In figure 5 (but not in subsequent figures), plots are extended in the $z$-direction one quarter-period beyond each periodic boundary to help visualize the flow in the turbulent region. The pattern wavelength is $\lambda_z=40$, so that $z=30$ and $z=-10$ describe the same point, as do $z=-30$ and $z=10$.

The mean flow can be described as follows. $U$ is strongest in the turbulent–laminar transition regions. In the transition region to the left of centre ($z=-10$) in figure 5, $U$ is negative and primarily in the upper half of the channel. To the right of centre ($z=10$), $U$ is positive and is seen primarily in the lower half of the channel. Comparison with turbulent kinetic energy shows that the transverse mean flow $U$ is out of phase with respect to the fluctuating field $\tilde{\boldsymbol{u}}$ by $\lambda_z/4$. This has been seen experimentally by Coles & Van Atta (1966) and Prigent *et al.* (2002, 2003, 2005).

The in-plane flow $\Psi$ in figure 5 has a large-aspect-ratio cellular structure consisting of alternating elliptical and hyperbolic points. The flow around the elliptical points, located in the centre of the turbulent regions, rotates in an anti-clockwise sense, opposing linear Couette flow. In the vicinity of the hyperbolic points, centred in the laminar regions, the in-plane deviation from linear Couette flow is very weak ($W$ and $V$ are nearly zero).

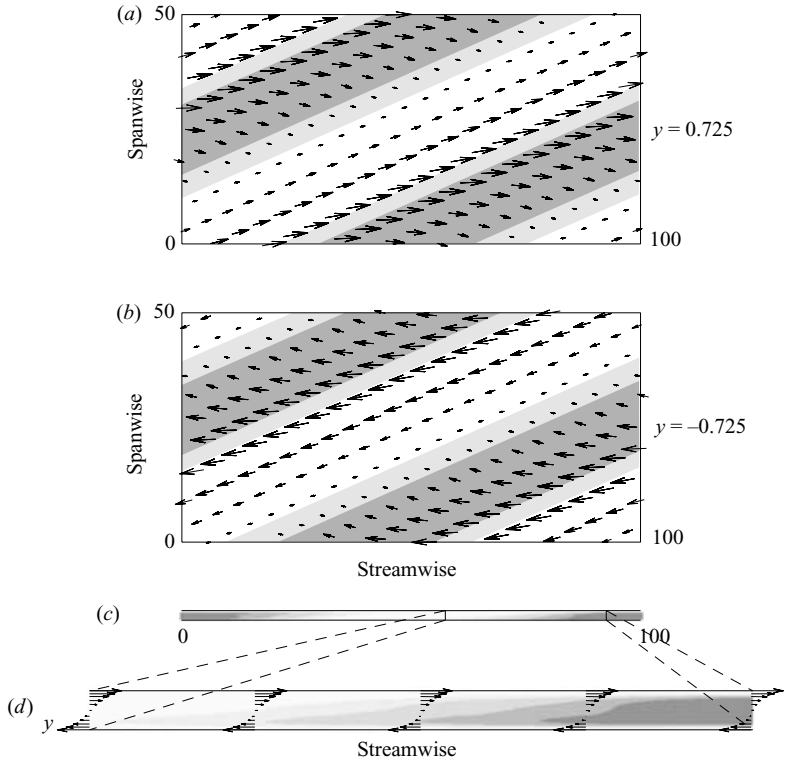


FIGURE 8. Mean velocity components seen in three planes with standard orientation for Couette flow. The turbulent regions are shaded. (*a*) Velocity components in the streamwise–spanwise plane at $y = 0.725$ (the upper part of the channel). (*b*) As (*a*) except $y = -0.725$ (the lower part of the channel). (*c*) Flow in a constant spanwise cut. The mean velocity is shown in the enlarged region (*d*).

Figure 6 shows $y$-profiles at four key points equally spaced along the pattern: centre of the laminar region, turbulent–laminar transition region, centre of the turbulent region, and the other turbulent–laminar transition region. While the $V$-profile is plotted, its variation is very small on the scale of $U$ and $W$ and can essentially be used to indicate the axis. Figure 7 shows profiles for the full mean flow $\langle \boldsymbol{u} \rangle = \boldsymbol{U} + \boldsymbol{u}^L$ containing the linear Couette profile.

The $U$-profiles in figure 7 are S-shaped, of the type found in turbulent Couette flow. This is to be expected in the turbulent region, even at these low Reynolds numbers. However, it is very surprising that the $U$-profile in the laminar region is also of this form. In the laminar region, local Reynolds stresses are absent (see figure 5) and so cannot be responsible for maintaining the S-shaped velocity profile in the laminar regions. The other prominent features in figures 6 and 7 are the asymmetric profiles at the transition regions.

The relationship between the mean flow field and the regions of turbulence can be seen in figure 8. Here the flow is shown in the standard orientations. In each view, the greyscale indicates the size of the turbulent energy and the arrows show the mean flow within the plane. In (*a*) and (*b*), the flow is shown in the streamwise–spanwise planes located at $y = 0.725$ and at $y = -0.725$. Figure 8(*c*) shows the flow between the plates, i.e. in a streamwise–cross-channel plane, and figure 8(*d*) shows an

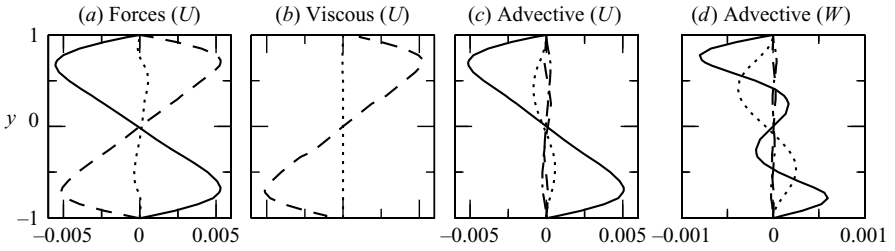


FIGURE 9. Balance of forces in the centre of the laminar region. (*a*) Forces in the $U$ direction. Advective terms (solid), viscous terms (dashed), Reynolds-stress terms (dotted). (*b*) Viscous terms in the $U$-direction. $(1/Re)\,\partial_y^2 U$ (dashed) dominates dominates $(1/Re)\,\partial_z^2 U$ (dotted). (*c*) Advective terms in the $U$-direction. Curves show $-\beta\, y\, \partial_z U$ (solid), $-W\partial_z U$ (dash-dotted), $-\alpha V$ (dotted), $-V\partial_y U$ (dashed). (*d*) Advective terms in the $W$-direction (for later reference). Curves show $-\beta\, y\, \partial_z W$ (solid), $-W\partial_z W$ (dash-dotted), $-\beta V$ (dotted), $-V\partial_y W$ (dashed).

enlargement of one of the laminar–turbulent transition regions. Note that the length $L_z = 40$ of our tilted computational domain corresponds to a streamwise length of $L_z/\sin\theta = 40/0.407 = 98.3 \approx 100$ and to a spanwise length of $L_z/\cos\theta = 43.78$.

The flow in figure 8 can be compared with the mean flow reported by Coles & Van Atta (1966) in experiments on turbulent spirals in Taylor–Couette flow. Coles and Van Atta measured the mean flow near the mid-gap between the rotating cylinders and noted an asymmetry between the mean flow into and out of turbulent regions. They found that the mean flow into turbulent regions was almost perpendicular to the turbulent–laminar interface whereas flow out of the turbulent region was almost parallel to the turbulent–laminar interface. We also observe a striking asymmetry between the mean flow into and out of the turbulent regions. The orientation of our mean flow does not agree in detail with that of Coles and Van Atta, but this is most likely due to the fact that Coles and Van Atta considered circular Taylor–Couette flow and measured the flow near the mid-gap. Referring to figures 5 and 6, one sees that the mid-plane ($y = 0$) is not the ideal plane on which to observe the mean flow since its structure is most pronounced between the mid-plane and the upper or lower walls.

Before considering the symmetries and force balances in detail, it is instructive to consider the dominant force balance just at the centre of the laminar region. Recall that one of the more interesting features of the mean flow is that the $U$-profile appears very similar to a turbulent profile, even in the absence of turbulence in the laminar region. Here the balance is dominated by advection and viscous diffusion, as shown in figure 9. Equation (2.13*a*) for flow in the $x$-direction is

$$0 = -(V\partial_y + (W+\beta y)\partial_z)(U+\alpha y) + \frac{1}{Re}\left(\partial_y^2 + \partial_z^2\right)U + F^U. \tag{3.2}$$

Variations in $y$ dominate variations in $z$, i.e. the usual boundary layer approximation $(\partial_y^2+\partial_z^2)U \simeq \partial_y^2 U$ holds; see, e.g., Pope (2000). Indeed, approximating the $y$-dependence of $U$ by the functional form $\sin(\pi y)$ suggested by figure 6, we have

$$O\left(\frac{\partial_y^2 U}{\partial_z^2 U}\right) = \frac{\pi^2}{k^2} = \frac{\pi^2}{(2\pi/40)^2} = 400. \tag{3.3}$$

This is confirmed by figure 9(*b*). In the centre of the laminar region $F^U$, $V$, and $W$ are all negligible, so that $-\beta y \partial_z U$ dominates the advective terms, as shown in figure 9(*c*).

Thus the balance between advection and viscosity in the laminar region is

$$\beta\, y\, \partial_z U \approx \frac{1}{Re}\partial_y^2 U. \tag{3.4}$$

This equation is appealingly simple and yet leads immediately to some interesting conclusions. The first is that a non-zero tilt angle $\theta$ is necessary to maintain the S-shaped $U$-profile in the laminar region, since otherwise $\beta = \sin\theta = 0$ and $U$ could be at most linear in $y$ and would in fact be zero, due to the homogeneous boundary conditions (2.14). The second conclusion follows from consideration of $y$-parity. The multiplication by $y$ on the left-hand side reverses $y$-parity, while the second derivative operator on the right-hand side preserves $y$-parity. The conclusion is that $U$ should be decomposed into odd and even components in $y$ and equation (3.4) should actually be understood as two equations coupling the two components. Specifically, as can be seen in figure 6, $U$ is odd in $y$ in the centre of the laminar region, yet $\partial_z U$ must be even for equation (3.4) to hold.

The remainder of the paper is devoted to formalizing, demonstrating and extending this basic idea.

### 3.2. *Symmetry and Fourier modes*

We now consider in depth the symmetry properties of the flow. We start with the symmetries of the system before averaging, that is, the Navier–Stokes equations (2.4) and boundary conditions (2.5). The system has translation symmetry in $x$ and $z$ as well as centrosymmetry under combined reflection in $x$, $y$ and $z$:

$$\kappa_{xyz}(u, v, w)(x, y, z) \equiv (-u, -v, -w)(x_0 - x, -y, z_0 - z), \tag{3.5}$$

where the origin $x_0$, $z_0$ can be chosen arbitrarily. Linear Couette flow $\boldsymbol{u}^L$ possesses all the system symmetries, as does the mean flow at Reynolds numbers for which turbulence is statistically homogeneous in $x$ and $z$.

Note that in the absence of tilt ($\theta = 0$), the system possesses two reflection symmetries. These can be taken to be $\kappa_{xyz}$ and reflection in the spanwise direction. For the tilted domain (at angles other than multiples of 90°), the only reflection symmetry is $\kappa_{xyz}$. This can be seen in figure 3(*a*): for general tilt angles $\theta$, spanwise reflection does not preserve the domain, i.e. does not leave the periodic boundaries in place. The experimental system shown in figure 1 possesses spanwise reflection symmetry and hence bands can be observed in the either of the two symmetrically related angles, the choice is dictated by factors such as initial conditions. By design, our tiled computational domain precludes the symmetry-related pattern given by spanwise reflection.

The transition to the turbulent–laminar patterned state breaks symmetry. Specifically, both the mean flow and the Reynolds-stress force break $z$-translation symmetry but break neither $x$-translation symmetry nor centrosymmetry. The spatial phase of the pattern in $z$ is arbitrary, but given a phase there are two values of $z_0$, separated by half a period, for which the flow is invariant under $\kappa_{xyz}$, as is typical for a circle pitchfork bifurcation (Crawford & Knobloch 1991). As can be seen in figure 5, the values of $z_0$ about which the patterns are centrosymmetric are the centres of the laminar ($z_0 = 0$) and of the turbulent ($z_0 = \pm 20$) regions.

The centrosymmetry operator for our averaged fields $\boldsymbol{U}$, which depend only on $y$ and $z$, is

$$\kappa_{yz}(U, V, W)(y, z) \equiv (-U, -V, -W)(-y, z_0 - z). \tag{3.6}$$

Since the Reynolds-stress force $(F^U, F^V, F^W)$ is centrosymmetric in the case we consider, then the averaged equations (2.13) for the mean field have centrosymmetry.

| | $z$ even | $z$ odd |
|---|---|---|
| $y$ even | 0.03% | 25.48% |
| $y$ odd | 74.48% | 0.01% |

TABLE 1. Energy $\int \mathrm{d}x \int \mathrm{d}y \int \mathrm{d}z\, |\boldsymbol{U}|^2/2$ of deviation from Couette flow contained in modes with different symmetries in $y$ and $z$. Modes with centrosymmetry (opposite parity in $y$ and $z$) contain $74.48\% + 25.48\% = 99.96\%$ of the total energy. Reflection in $z$ is about the centre of the laminar region.

| | $z$ even (cosine) | | | $z$ odd (sine) | |
|---|---|---|---|---|---|
| $z$ wavenumber | 0 | $k$ | $\geqslant 2k$ | $k$ | $\geqslant 2k$ |
| $y$ even | | | | 25.2% | 0.3% |
| $y$ odd | 69.7% | 4.7% | 0.1% | | |

TABLE 2. Energy contained in $z$ Fourier modes. Modes retained (in boxes) are $\boldsymbol{U}_0(y)$, $\boldsymbol{U}_c(y)\cos(kz)$ and $\boldsymbol{U}_s(y)\sin(kz)$. These contain $69.7\% + 4.7\% + 25.2\% = 99.6\%$ of the total energy.

We formalize this further as follows. Any $x$-independent field $\boldsymbol{g}$ can be decomposed into even and odd functions of $y$ and $z$ as

$$\boldsymbol{g}(y, z) = \boldsymbol{g}_{oo}(y, z) + \boldsymbol{g}_{oe}(y, z) + \boldsymbol{g}_{eo}(y, z) + \boldsymbol{g}_{ee}(y, z) \tag{3.7}$$

where, for example, $\boldsymbol{g}_{oe}$ is odd in $y$ and even in $z - z_0$. Applying the operator in (3.6) to (3.7), we obtain

$$\begin{aligned}\kappa_{yz}\boldsymbol{g}(y, z) &= -\boldsymbol{g}_{oo}(-y, z_0 - z) - \boldsymbol{g}_{oe}(-y, z_0 - z) - \boldsymbol{g}_{eo}(-y, z_0 - z) - \boldsymbol{g}_{ee}(-y, z_0 - z) \\ &= -\boldsymbol{g}_{oo}(y, z) + \boldsymbol{g}_{oe}(y, z) + \boldsymbol{g}_{eo}(y, z) - \boldsymbol{g}_{ee}(y, z).\end{aligned} \tag{3.8}$$

For the field $\boldsymbol{g}$ to be centrosymmetric requires $\kappa_{yz}\boldsymbol{g} = \boldsymbol{g}$, so that in fact

$$\boldsymbol{g}(y, z) = \boldsymbol{g}_{oe}(y, z) + \boldsymbol{g}_{eo}(y, z). \tag{3.9}$$

Table 1, as well as figure 5, shows that this is indeed the case for $\boldsymbol{U}$; it holds for $\boldsymbol{F}$ as well.

We now Fourier-transform in $z$ to further decompose the mean velocity and the Reynolds-stress force. We find that the $z$-wavenumbers 0 and $\pm k$ have contributions to $\boldsymbol{U}$ which are an order of magnitude higher than the remaining wavenumber combinations. See table 2. The deviation from the $z$ average is thus almost exactly trigonometric, with almost no higher harmonic content. The dominance of these terms in the Fourier series means that $\boldsymbol{U}$ and $\boldsymbol{F}$ can be represented by only three functions of $y$, namely,

$$\boldsymbol{g}(x, y, z) = \boldsymbol{g}_0(y) + \boldsymbol{g}_c(y)\cos(kz) + \boldsymbol{g}_s(y)\sin(kz), \tag{3.10}$$

which is a special case of (3.9), with the first two terms of (3.10) coinciding with $\boldsymbol{g}_{oe}(y, z)$ and the last with $\boldsymbol{g}_{eo}$. Thus, $\boldsymbol{g}_0$ and $\boldsymbol{g}_c$ are odd functions of $y$, while $\boldsymbol{g}_s$ is even. The fields thus consist of a $z$-independent component $\boldsymbol{g}_0$ and two components which vary trigonometrically and out of phase with one another, $\boldsymbol{g}_c$ dominating in the laminar and turbulent regions and $\boldsymbol{g}_s$ dominating in the boundaries between them. Moreover, $\boldsymbol{g}_s$ dominates in the bulk, since $\boldsymbol{g}_0$ and $\boldsymbol{g}_c$ are odd in $y$ and thus zero in the channel centre.

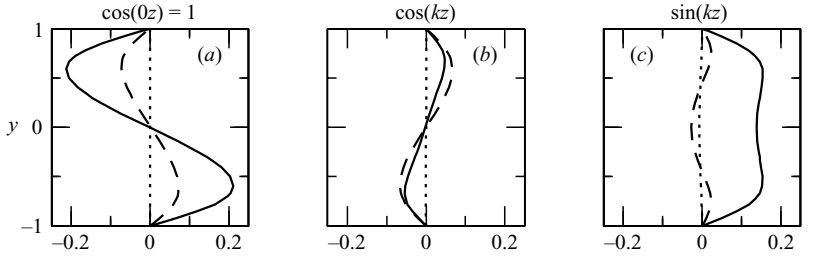


FIGURE 10. Fourier decomposition of mean velocity. $U$-component (solid), $V$-component (dotted), $W$-component (dashed). $W_c \approx -W_0$, corresponding to the fact that $W$ shows no deviation from the linear in the laminar region.

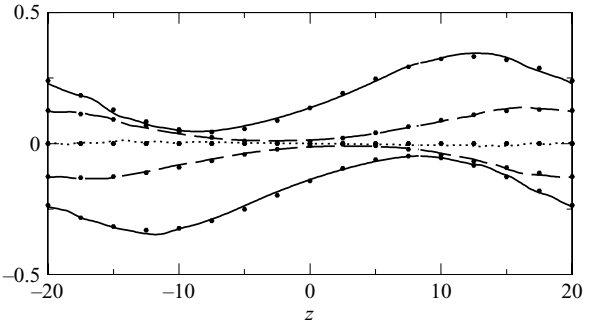


FIGURE 11. Mean flow as a function of $z$ at $y = 0.725$ (lower curves) and $y = -0.725$ (upper curves). $U$ (solid), $V$ (dotted), $W$ (dashed). Points show values calculated from trigonometric formula (3.10).

That is,

$$\boldsymbol{g} = \boldsymbol{g}_0(y) + \boldsymbol{g}_c(y),\ z = 0\text{: centre of laminar region,} \tag{3.11a}$$

$$\boldsymbol{g} = \boldsymbol{g}_0(y) + \boldsymbol{g}_s(y),\ z = \lambda_z/4 = 10\text{: laminar–turbulent boundary,} \tag{3.11b}$$

$$\boldsymbol{g} = \boldsymbol{g}_0(y) - \boldsymbol{g}_c(y),\ z = \lambda_z/2 = 20\text{: centre of turbulent region,} \tag{3.11c}$$

$$\boldsymbol{g} = \boldsymbol{g}_0(y) - \boldsymbol{g}_s(y),\ z = 3\lambda_z/4 = 30\text{: turbulent–laminar boundary.} \tag{3.11d}$$

Figure 10 shows the three trigonometric components, each a function of $y$, obtained by Fourier-transforming $U$, $V$, and $W$. Figure 11 shows $U$, $V$ and $W$ as functions of $z$ at locations in the upper and lower channel and compares them with the values obtained from the trigonometric formula (3.10) using the functions shown in figure 10. Figures 12, 13 and 14 depict $U(y, z)$, $\Psi(y, z)$ and $F^U(y, z)$ with their trigonometric decompositions. Each of these figures uses only the three scalar functions of $y$, figure 10, to reproduce the corresponding two-dimensional field. As shown by (2.15), the stream-function $\Psi$ of a centrosymmetric field has symmetry opposite to that of the velocity components, i.e. it is composed of functions of the same parity in $y$ and $z$.

Figures 15 and 16 show the three Reynolds-stress forces and their Fourier decompositions. Each component obeys $F_c \approx -F_0$, a necessary condition for $\boldsymbol{F}$ to vanish at the centre of the laminar region, as shown by (3.11$a$) and also illustrated in figure 14. More precisely,

$$F_c^U = -1.09F_0^U, \quad F_c^V = -1.22F_0^V, \quad F_c^W = -1.16F_0^W. \tag{3.12}$$

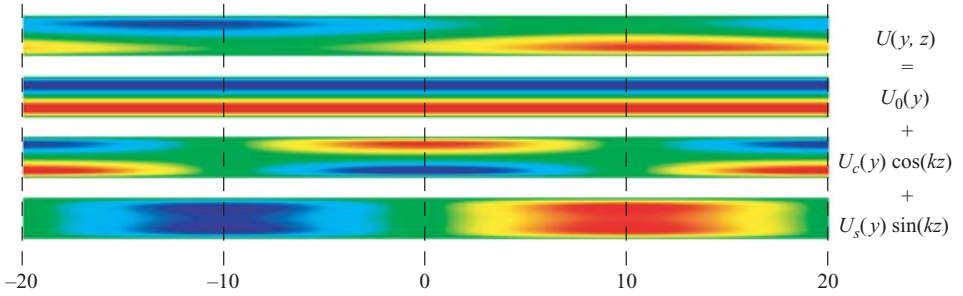


FIGURE 12. Mean velocity $U$ and its trigonometric decomposition. Because the magnitude of the fields vary, different colour scales are chosen to emphasize qualitative features. $U$ $[-0.2, 0.2]$, $U_0$ $[-0.2, 0.2]$, $U_c$ $[-0.05, 0.05]$, $U_s$ $[-0.154, 0.154]$.

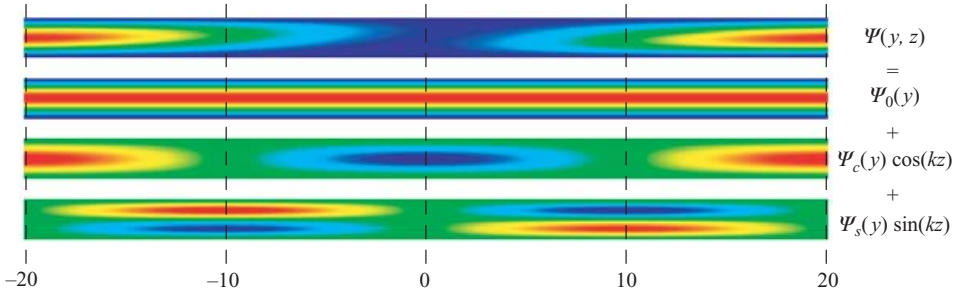


FIGURE 13. Mean streamfunction $\Psi(y, z)$ for deviation of in-plane flow from linear Couette flow and its trigonometric decomposition. Colour scale is $\Psi$ $[0, 0.09]$, $\Psi_0$ $[0, 0.046]$, $\Psi_c$ $[-0.042, 0.042]$, $\Psi_s$ $[-0.008, 0.008]$.

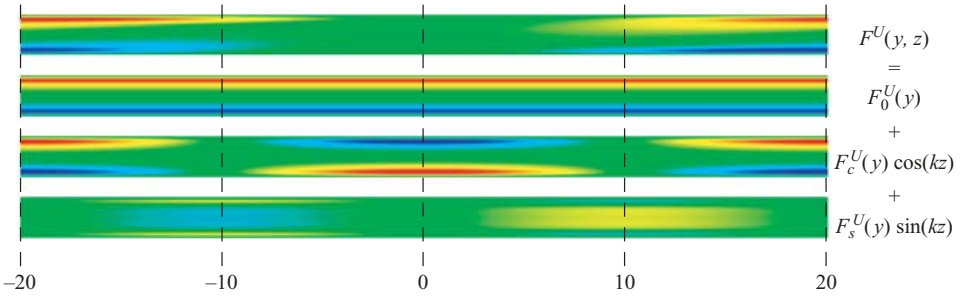


FIGURE 14. Reynolds-stress force $F^U$ and its trigonometric decomposition. Colour scale is $F^U$ $[-0.017, 0.017]$, $F^U_0$ $[-0.0085, 0.0085]$, $F^U_c$ $[-0.0085, 0.0085]$, $F^U_s$ $[-0.0085, 0.0085]$.

In addition,

$$\boldsymbol{F} \approx -\partial_y \langle \tilde{\boldsymbol{u}} \tilde{v} \rangle. \tag{3.13}$$

as is typical for turbulent channel flows; see e.g. Pope (2000).

### 3.3. *Force balance for U*

We now turn to investigating the balance of forces responsible for maintaining the mean flow profiles. We focus primarily on $U$, both because it is the component of largest amplitude and also because it appears only in (2.13*a*): $U$ is subject to Reynolds-stress and viscous forces, and is advected by $(V, W)$ but is not self-advected. We begin

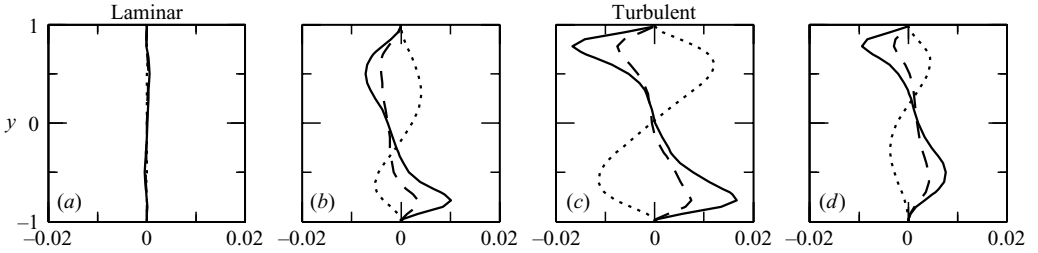


FIGURE 15. Reynolds-stress force $\boldsymbol{F} = -\langle(\tilde{\boldsymbol{u}}\cdot\nabla)\tilde{\boldsymbol{u}}\rangle$ as a function of $y$. Curves show $F^U$ (solid), $F^V$ (dotted) and $F^W$ (dashed).

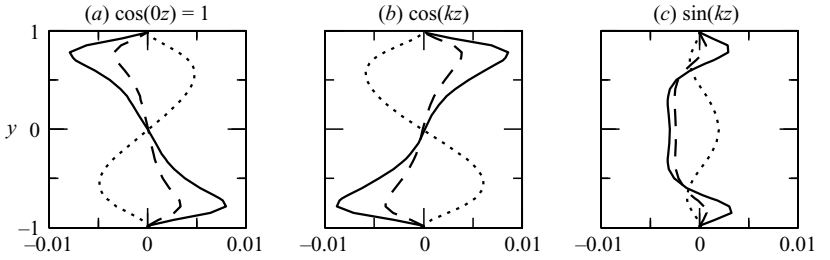


FIGURE 16. Fourier decomposition of Reynolds-stress force. $F^U$-components (solid), $F^V$-components (dotted), $F^W$-components (dashed). $\boldsymbol{F}_c \approx -\boldsymbol{F}_0$, as required for the vanishing of $\boldsymbol{F}$ at $z = 0$.

by showing the balance of forces in the $U$-direction as a function of $z$ at locations in the upper and lower channel in figure 17. One can again see the centrosymmetry of each of the forces, i.e. invariance under the combined operations of reflection in $y$ and $z$ and change of sign. The Reynolds-stress force disappears at the centre of the laminar region and the advective and viscous forces exactly counter-balance, as emphasized in the figures on the right. Figure 18 shows another view of this balance, displaying the forces as a function of $y$ at four locations in $z$. As previously stated, $\nabla^2 U$ is dominated by $\partial_y^2 U$ and $F^U$ by $-\partial_y\langle\tilde{u}\tilde{v}\rangle$. In figure 19, we show the Fourier-space analogue of figure 18.

We now turn to the more complex advective forces, whose Fourier decompositions are shown in figure 20. The cos(0$z$)-component of the advective force is small but non-zero. Because this term results from the product of trigonometric functions, it also provides a measure of the generation of higher harmonics, a point which we will explore further in § 3.5. The advective cos($kz$) term is well approximated by the contribution from advection by $w^L = \beta y$. The advective sin($kz$) term is dominated near the walls by advection by $w^L$, but in the bulk by advection by $V$. Properties of the cos($kz$) and sin($kz$) modes echo their physical space counterparts: the advective term is well approximated by advection by $w^L$ in the laminar region, as was shown in figure 9, while the advective forces in the laminar–turbulent boundaries combine advection by $w^L$ near the walls and by $V$ in the bulk.

We illustrate these conclusions via schematic visualizations of the dynamics of $U$. Figure 21 illustrates the dynamics in the laminar and turbulent regions. The dynamics in the laminar region are essentially described by the simple balance between viscous diffusion of $U$ profiles and advection by linear Couette flow in $z$, given by (3.4). Viscous diffusion tends to reduce curvature, but the profiles have greater curvature upstream (to the left for the upper channel, to the right for the lower channel).

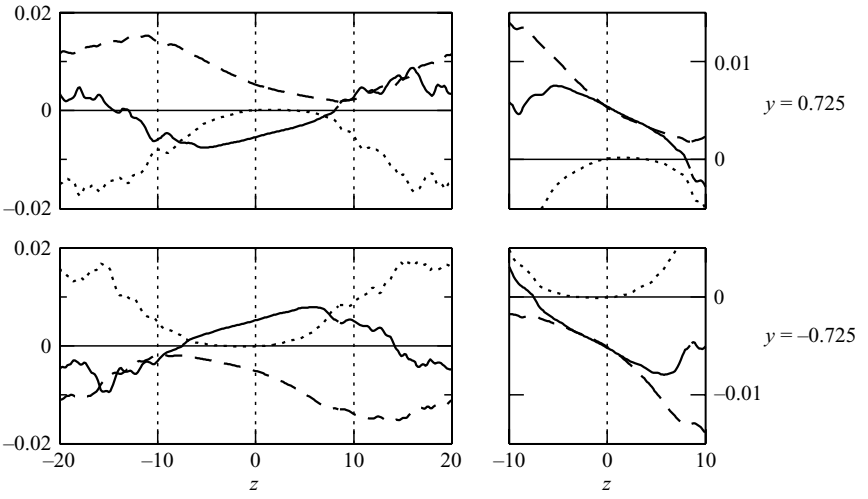


FIGURE 17. Balance of forces in the $U$-direction as a function of $z$ at $y = \pm 0.725$ for turbulent–laminar pattern at $Re = 350$. Advective $-(\boldsymbol{U}\cdot\nabla)U$ (solid), viscous $\nabla^2 U$ (dashed), and turbulent $-\langle(\tilde{\boldsymbol{u}}\cdot\nabla)\tilde{u}\rangle$ (dotted) forces. In the laminar region ($z \approx 0$), the Reynolds-stress force vanishes and the viscous and advective forces are equal and opposite to one another. In the figures on the right, enlarged around the laminar region, $\nabla^2 U$ and $+(\boldsymbol{U}\cdot\nabla)U$ are shown to emphasize equality between viscous and advective forces.

Hence advection replenishes the curvature damped by viscosity. However, this trend towards greater curvature upstream cannot continue indefinitely, since the pattern is periodic in $z$. Hence eventually a maximum is reached (at a turbulent–laminar boundary), beyond which the curvature decreases upstream. Thus, in the turbulent region, advection and diffusion act together to decrease curvature and must both be counter-balanced by turbulent forcing. These features are essentially described by the $\cos(0z) = 1$ and $\cos(kz)$ modes. Figure 22 illustrates the dynamics in the turbulent–laminar boundaries. These dynamics include advection by $V$ in the bulk, leading to the $U > 0$ ($U < 0$) patch in the lower right (upper left) of figure 12 and are described by the $\sin(kz)$ mode.

### 3.4. *Force balance for W and V*

Figure 23 shows the balance of forces in the $W$-direction and figure 24 its analogue in Fourier space. This balance resembles that in the $U$-direction shown in figures 18 and 19. In physical space (compare figure 23*a* and figure 18*a*), the main difference is that the advective and viscous forces are both small in the laminar region, in keeping with the fact that $W \approx 0$. The pressure gradient $\partial_z P$ is far smaller than the other forces throughout (see below). In Fourier space (compare figure 24*b* and figure 19*b*), the main difference with the $U$ balance is that the relative importance of the viscous and advective forces in the $\cos(kz)$ balance is reversed from that in the case of $U$: for $W$, the viscous component is larger than the advective component, which is especially small in the bulk. The decomposition of the advective terms (figure 25) shows that, as is the case for $U$, the advective $\cos(kz)$ term is well approximated by the contribution from advection by $w^L = \beta y$, whereas all four advective components contribute to the $\sin(kz)$ term.

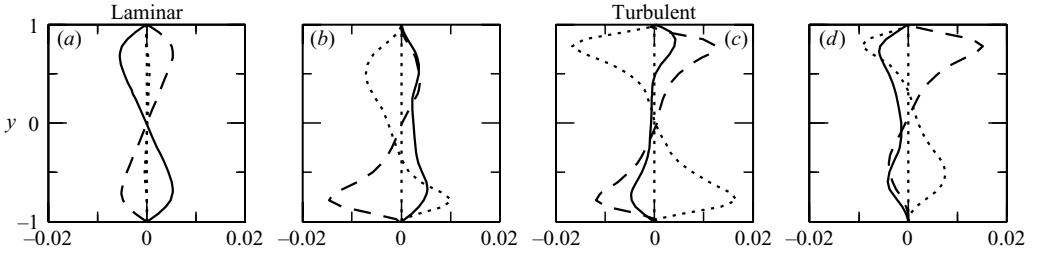


FIGURE 18. Balance of forces in the $U$-direction. Curves show advective force (solid), viscous force (dashed) and Reynolds-stress force (dotted). In the laminar region, the Reynolds-stress force is negligible and the advective and viscous forces counter-balance one another.

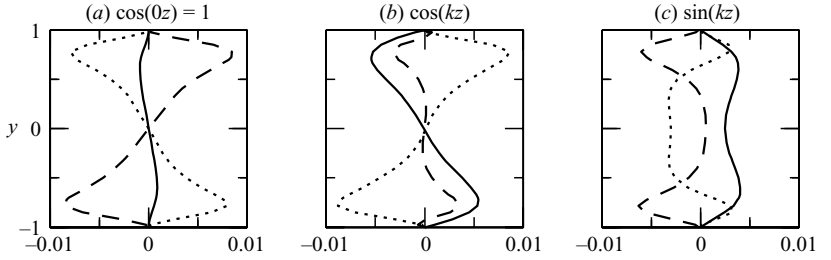


FIGURE 19. Balance of forces in the $U$-direction, decomposed into modes. Curves show advective (solid), viscous (dashed) and Reynolds-stress (dotted) forces. Constant mode: Reynolds-stress and viscous forces approximately counter-balance each other. Mode $\cos(kz)$: advection is larger than viscous force, which is especially small in the bulk.

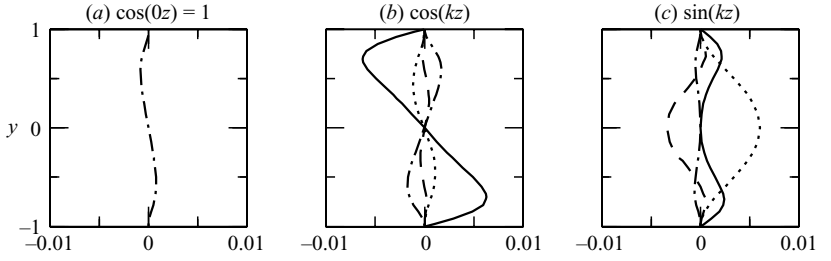


FIGURE 20. Advective terms in the $U$-direction, decomposed into modes. Curves show $-\beta y \partial_z U$ (solid) $-W\partial_z U$ (dash-dot), $-\alpha V$ (dotted), $-V\partial_y U$ (dashed). The constant mode is generated by the product $-kW_cU_s/2$; a second harmonic of the same small size is also generated. The $\cos(kz)$ mode is dominated by $-\beta\, y\, k\, U_s$. The $\sin(kz)$ term is dominated by $\beta\, y\, k\, U_c$ near the boundaries and by $-V_s\partial_y(U_0 + \alpha y)$ in the bulk.

The balance of forces in the $V$-direction is entirely different. The dominant balance in this equation is

$$0 = -\partial_y P + F^V, \tag{3.14}$$

as shown in figure 26. This is typical for turbulent channel flows; see e.g. (Pope 2000). This balance between the mean pressure gradient $P$ and the Reynolds-stress force $F^V$ does not constrain or provide information about any of the velocity components. Since

$$F^V = -\boldsymbol{\nabla}\cdot\langle\tilde{\boldsymbol{u}}\tilde{v}\rangle \approx -\partial_y\langle\tilde{v}^2\rangle, \tag{3.15}$$

we in fact have

$$P \approx -\langle\tilde{v}^2\rangle \tag{3.16}$$

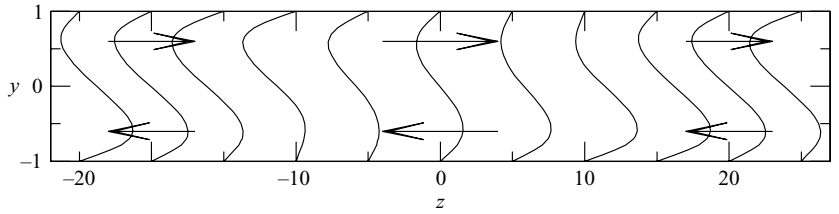


FIGURE 21. Schematic depiction of the dynamics of $U$ near the centres of the laminar and of the turbulent regions. The cross-channel direction is exaggerated. $U$ (profiles) and $W+\beta y$ (arrows) are shown. Viscous diffusion tends to diminish both peaks of the profile. In the laminar region surrounding $z=0$, the peaks in the upper half-channel increase in amplitude with decreasing $z$; advection towards positive $z$ (upper arrow) replenishes these peaks, maintaining $U$. Conversely, the peaks in the lower half-channel increase with $z$; advection towards negative $z$ (lower arrow) replenishes these peaks. That is, the sign of $-(W+\beta y)\,\partial_z U$ is opposite to that of $\partial_y^2 U$ in both the upper and lower parts of the laminar region. In the turbulent region around $z=\pm 20$, the size of the upper (lower) peak decreases to the left (right) and so advection, like viscous diffusion, acts instead to diminish the peaks. $U$ is maintained by the Reynolds-stress force, which counter-balances both. The effect is to modulate the amplitude of the $U$-profiles periodically in $z$.

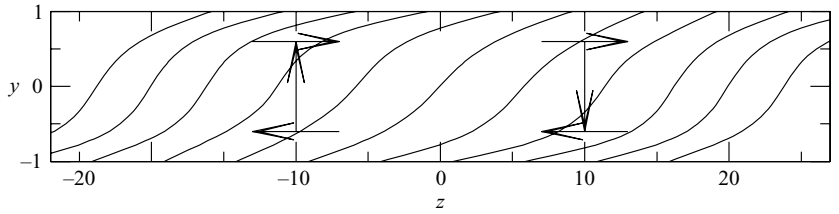


FIGURE 22. Schematic depiction of the dynamics of $U$ near the turbulent–laminar boundaries. The cross-channel direction is exaggerated. $U+\alpha y$ (profiles) and $(V, W+\beta y)$ (arrows) are shown. Near the upper and lower walls, the $U+\alpha y$-profiles are advected towards increasing/decreasing $z$ by $W+\beta y$. In the bulk, advection by $V$ is significant. At $z\approx 10$, $V$ advects downwards the right-moving fluid in the upper portion of the channel. At $z\approx -10$, $V$ advects upwards the left-moving fluid in the lower portion of the channel. The effect is to tilt the $U=0$ boundary periodically in $z$.

up to a small $z$-dependent correction. Figure 5 shows the pressure field $P$ calculated from (3.16) and suggests that its $y$-dependence can be approximated by the functional form $\cos(\pi y/2)$. This leads to an estimate of the relative importance of the pressure gradients in the $y$- and $z$-directions:

$$O\left(\frac{\partial_y P}{\partial_z P}\right) = \frac{\pi/2}{k} \approx 10, \tag{3.17}$$

while our data show

$$\frac{(\partial_y P)_{\max}}{(\partial_z P)_{\max}} = \frac{0.012}{0.0017} = 7.05. \tag{3.18}$$

The same estimate applies to the relative magnitudes of $V$ and $W$, using the streamfunction shown in figure 5,

$$O\left(\frac{W}{V}\right) = O\left(\frac{\partial_y \Psi}{\partial_z \Psi}\right) = \frac{\pi/2}{2\pi/40} = 10, \tag{3.19}$$

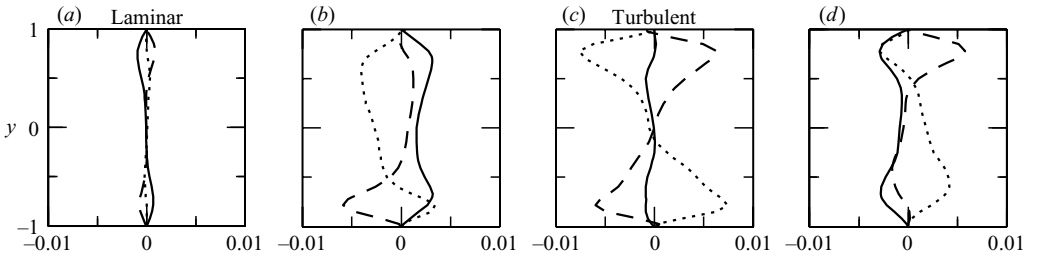


FIGURE 23. Balance of forces in the $W$-direction. Curves show advective term (solid), viscous force (dashed) and Reynolds-stress force (dotted). In the laminar region, $W \approx 0$ and each of the forces is negligible. In the turbulent region, the viscous and Reynolds-stress forces counter-balance one another. In the laminar–turbulent boundaries, the advective, viscous and Reynolds-stress forces all play a role.

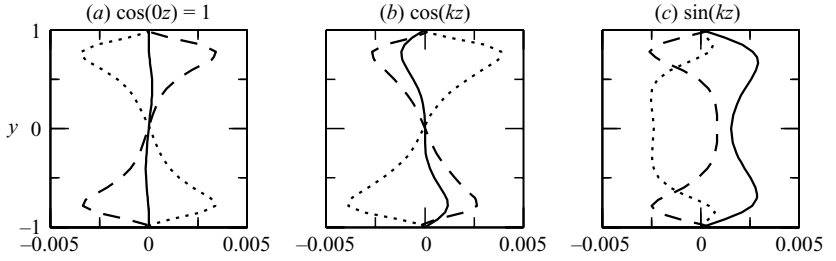


FIGURE 24. Balance of forces in the $W$ direction, decomposed into modes. Curves show advective term (solid), viscous term (dashed) and turbulent forcing term (dotted).

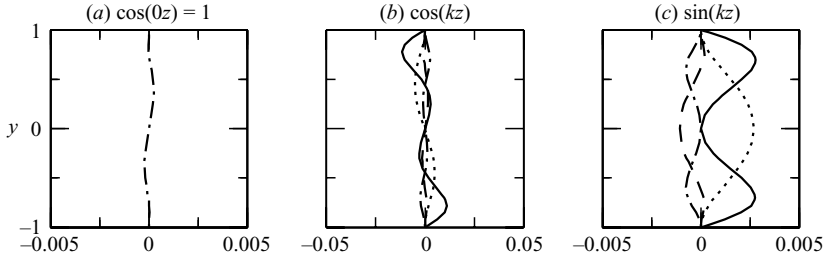


FIGURE 25. Advective terms in the $W$-direction, decomposed into modes. Curves show $-\beta y \partial_z W$ (solid) $-W\partial_z W$ (dash-dotted), $-\beta V$ (dotted), $-V\partial_y W$ (dashed). The $\cos(kz)$ mode is dominated by $-\beta\, y\, k\, W_s$. The $\sin(kz)$ term is dominated by $\beta\, y\, k\, W_c$ near the boundaries and by $-V_s \partial_y (W_0 + \beta y)$ in the bulk.

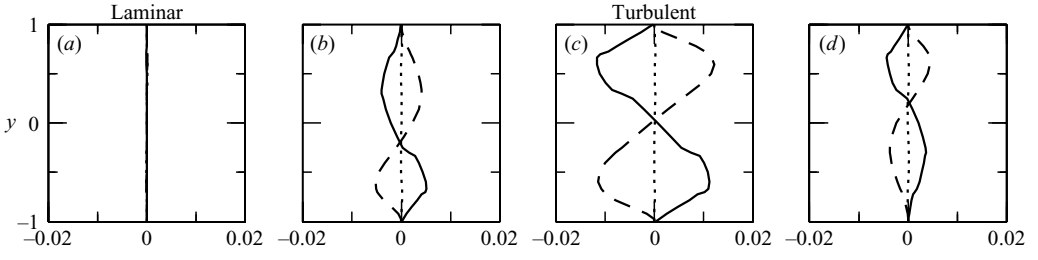


FIGURE 26. Forces in the $V$-direction. Reynolds-stress force $F^V$(dashed) is counter-balanced by pressure gradient $-\partial_y P$ (solid). Both are zero in the laminar region. Advective and viscous forces (dotted) are negligible throughout.

while the actual ratio of maximum values is

$$\frac{W_{\max}}{V_{\max}} = \frac{0.15}{0.013} = 11. \tag{3.20}$$

### 3.5. *Model equations*

We now derive a system of ordinary differential equations by substituting the trigonometric form (3.10) into the Reynolds-averaged Navier–Stokes equations (2.13). The drawback in this procedure is the usual one, namely that this form is not preserved by multiplication. However, table 2 shows that higher harmonics contribute very little to $\boldsymbol{U}$.

We expand the advective term as:

$$\begin{aligned}((\boldsymbol{U}+\boldsymbol{u}^L)\cdot\nabla)(\boldsymbol{U}+\boldsymbol{u}^L) &= (V\,\partial_y + (W+\beta y)\,\partial_z)(\boldsymbol{U}+\alpha y\boldsymbol{e}_x+\beta y\boldsymbol{e}_z)\\ &= (V_c\cos(kz)+V_s\sin(kz))(\boldsymbol{U}'_0+\boldsymbol{U}'_c\cos(kz)+\boldsymbol{U}'_s\sin(kz)+\alpha\boldsymbol{e}_x+\beta\boldsymbol{e}_z)\\ &\quad+(W_0+\beta y+W_c\cos(kz)+W_s\sin(kz))(-k\,\boldsymbol{U}_c\sin(kz)+k\,\boldsymbol{U}_s\cos(kz)) \qquad (3.21a)\\ &= \frac{1}{2}(V_c\,\boldsymbol{U}'_c+V_s\,\boldsymbol{U}'_s+k\,(W_c\,\boldsymbol{U}_s-W_s\,\boldsymbol{U}_c))\\ &\quad+(V_c(\boldsymbol{U}'_0+\alpha\boldsymbol{e}_x+\beta\boldsymbol{e}_z)+k\,(W_0+\beta y)\boldsymbol{U}_s)\cos(kz)\\ &\quad+(V_s(\boldsymbol{U}'_0+\alpha\boldsymbol{e}_x+\beta\boldsymbol{e}_z)-k\,(W_0+\beta y)\boldsymbol{U}_c)\sin(kz)\\ &\quad+\tfrac{1}{2}(V_c\,\boldsymbol{U}'_c-V_s\,\boldsymbol{U}'_s+k\,(W_c\,\boldsymbol{U}_s+W_s\,\boldsymbol{U}_c))\cos(2kz), \qquad (3.21b)\end{aligned}$$

where primes denote $y$ differentiation. We neglect the second harmonic term in the lastline of (3.21*b*), and will discuss the accuracy of this approximation below. We now rewrite the $U$- and $W$-components of the averaged momentum equations, neglecting the $z$-derivatives $\partial_z^2 U$, $\partial_z^2 W$ and $\partial_z P$, as justified by equations (3.3) and (3.17):

$$0 = -(V\partial_y + (W+\beta y)\,\partial_z)(U+\alpha y) + \frac{1}{Re}\partial_y^2 U + F^U, \tag{3.22a}$$

$$0 = -\left(V\partial_y + (W+\beta y)\,\partial_z\right)(W+\beta y) + \frac{1}{Re}\partial_y^2 W + F^W \tag{3.22b}$$

Substituting the first three lines of (3.21*b*) in (3.22) and separating terms in $\cos(0z)=1$, $\cos(kz)$ and $\sin(kz)$, we obtain

$$0 = -\tfrac{1}{2}[V_c U'_c + V_s U'_s + k(W_c U_s - W_s U_c)] + \frac{1}{Re}U''_0 + F^U_0, \tag{3.23a}$$

$$0 = -V_c(U'_0+\alpha) - k\,(W_0+\beta y)U_s + \frac{1}{Re}U''_c + F^U_c, \tag{3.23b}$$

$$0 = -V_s(U'_0+\alpha) + k\,(W_0+\beta y)U_c + \frac{1}{Re}U''_s + F^U_s, \tag{3.23c}$$

$$0 = -\tfrac{1}{2}[V_c W'_c + V_s W'_s] + \frac{1}{Re}W''_0 + F^W_0, \tag{3.23d}$$

$$0 = -V_c(W'_0+\beta) - k\,(W_0+\beta y)W_s + \frac{1}{Re}W''_c + F^W_c, \tag{3.23e}$$

$$0 = -V_s(W'_0+\beta) + k\,(W_0+\beta y)W_c + \frac{1}{Re}W''_s + F^W_s, \tag{3.23f}$$

where the Fourier modes of $V$ and $W$ are related via those of the streamfunction $\Psi$ of (2.15):

$$V_0 = 0, \quad W_0 = \Psi'_0, \tag{3.24a}$$

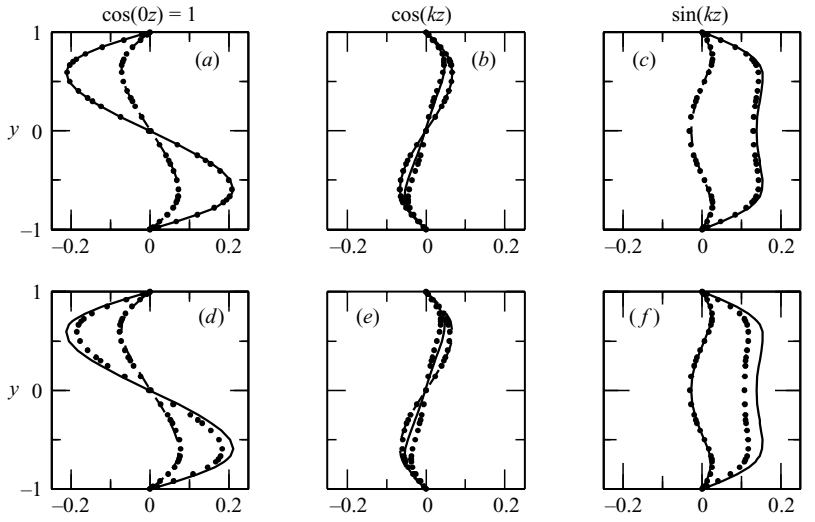


FIGURE 27. Comparison between mean velocities (in Fourier representation) from full DNS and ODE models. (*a*), (*b*), (*c*): Curves show $U$ (solid) and $W$ (dashed) from DNS. Dots show solution to the full ODE model (3.23), essentially indistinguishable from the solid curves. (*d*), (*e*), (*f*): Curves again show $U$ (solid) and $W$ (dashed) from DNS. Dots show solution to simplified ODE model (3.26). The agreement with DNS is very good, though there are small differences particularly in the $U$-component.

$$V_c = -k\Psi_s, \quad W_c = \Psi_c', \tag{3.24b}$$

$$V_s = k\Psi_c, \quad W_s = \Psi_s', \tag{3.24c}$$

and where homogeneous boundary conditions are imposed:

$$0 = U_0 = U_c = U_s \quad \text{at } y = \pm 1, \tag{3.25a}$$

$$0 = W_0 = W_c = W_s \quad \text{at } y = \pm 1. \tag{3.25b}$$

System (3.23) with boundary conditions (3.25) is composed of six ordinary differential equations coupling the six scalar functions $U_0, U_c, U_s, \Psi_0, \Psi_c, \Psi_s$ of $y$, with six turbulent forces $F_0^U, F_c^U, F_s^U, F_0^W, F_c^W, F_s^W$.

We have solved (3.23)–(3.25) numerically, using as inputs $F^U$ and $F^W$ obtained from our full simulations, i.e. the $\boldsymbol{F}$ modes shown in figure 16. The resulting solutions are shown in figure 27. For comparison, we reproduce from figure 10 the mean velocity fields, in Fourier representation, from our full simulations (DNS). The ODE solutions are virtually indistinguishable from the mean fields from DNS. Only in the sine component of $U$ can the ODE solutions be distinguished (and only very slightly) from the DNS results. From the profiles in figure 27, the full mean fields could be constructed as in figures 12 and 13. Thus, while the ODE model requires input of the Reynolds-stress force terms, $F^U$ and $F^W$, it demonstrates the simplicity of the force balance responsible for generating the patterned flow when viewed in the Fourier representation. Considering higher harmonics would be straightforward, but would serve little purpose.

We can go in the other direction and attempt to simplify system (3.23). The approximate equalities $F_c^U \approx -F_0^U$, $F_c^W \approx -F_0^W$ (see equation (3.12)), necessary for $\boldsymbol{F}$ to vanish at the centre of the laminar region, can be imposed exactly, reducing the number of turbulent forcing input functions to four. The terms arising from the

advective forces can be reduced by making approximations justified from figures 20 and 25. The nonlinear terms in (3.23*a*) and (3.23*d*) can be neglected. The advective terms in (3.23*b*) and (3.23*e*) can be approximated by $-k\,\beta\,y\,U_s$ and $-k\,\beta\,y\,W_s$. Making these approximations, we obtain:

$$0 = \frac{1}{Re}U_0'' + F_0^U, \tag{3.26a}$$

$$0 = -k\,\beta\,y\,U_s + \frac{1}{Re}U_c'' - F_0^U, \tag{3.26b}$$

$$0 = -V_s(U_0' + \alpha) + k(W_0 + \beta y)U_c + \frac{1}{Re}U_s'' + F_s^U, \tag{3.26c}$$

$$0 = \frac{1}{Re}W_0'' + F_0^W, \tag{3.26d}$$

$$0 = -k\,\beta\,y\,W_s + \frac{1}{Re}W_c'' - F_0^W, \tag{3.26e}$$

$$0 = -V_s(W_0' + \beta) + k(W_0 + \beta y)W_c + \frac{1}{Re}W_s'' + F_s^W. \tag{3.26f}$$

The solutions to this simplified ODE model are also presented in figure 27. There is quite good agreement with full DNS results, thus demonstrating that the dominant force balance is captured by this very simple system of ODEs. We stress that the only nonlinearities in this model are in (3.26*c*) and (3.26*f*). This reflects the complexity of the dynamics in the turbulent–laminar boundaries regions (and the simplicity of the dynamics in the centre of the turbulent and laminar regions.)

From the simplified ODE model we can obtain the approximate equation satisfied at the centre of the laminar region by adding (3.26*a*) and (3.26*b*):

$$k\,\beta\,y\,U_s = \frac{1}{Re}(U_0 + U_c)''. \tag{3.27}$$

This is a restatement in terms of Fourier components of the balance described by (3.4) and figure 9.

## 4. Discussion

We have presented an analysis of a particular turbulent–laminar pattern obtained in simulations of large-aspect-ratio plane Couette flow. We have focused on a single example so as to understand in quantitative detail the structure of these unusual flows. The key findings obtained in our study are as follows. First we find that in the (quasi-) laminar flow region the velocity profiles are not simply those of linear Couette flow. Instead a non-trivial flow is maintained in the laminar regions by a balance between viscous diffusion and nonlinear advection. Next we have considered the symmetries of the flow. When the pattern forms, the time-averaged flow breaks the translation symmetry but not centrosymmetry. The patterned state is centrosymmetric about the centre of the laminar region and about the centre of the turbulent region. Next we have considered a spatial Fourier decomposition of the mean flow in the direction of the pattern wavevector. From this we find that the lateral structure of the pattern is almost completely harmonic, i.e. composed of a constant and single harmonic. Thus the pattern description can be reduced to just three cross-channel functions for each field, in that $\boldsymbol{U}(x, y, z) \approx \boldsymbol{U}_0(y) + \boldsymbol{U}_c(y)\cos(kz) + \boldsymbol{U}_s(y)\sin(kz)$. The absence of higher harmonics suggests that the pattern is near the threshold, in some sense, of a linear instability of a uniform turbulent state. Such an instability would be governed

by a linear equation with coefficients which are constant in $z$, whose solutions are necessarily trigonometric in $z$.

From our analysis of the turbulent–laminar pattern, in particular its Fourier decomposition, we derive a model which reproduces the patterned flow. The model is derived from the averaged Navier–Stokes equations with the following assumptions. The crucial assumption, which is strongly supported by our numerical computations, is that the mean flow can be expressed in terms of just three horizontal modes. Effectively the generation of higher harmonics via nonlinear terms in the Navier–Stokes equations is negligible in the mean flow. The model is then further simplified because viscous diffusion is dominated by cross-channel diffusion – the standard boundary layer approximation – and because pressure variation is negligible along the pattern wavevector. We take as input to the model the Reynolds-stress forces measured from computations. Assuming that the Reynolds stresses exactly vanish in the centre of the laminar regions, the number of inputs to the model is just four cross-channel functions. The result is a system of six simple ordinary differential equations which depend on four forcing functions. The model equations accurately reproduce the mean flow from full direct numerical simulations.

A number of other researchers have attempted to reduce the description of turbulent or transitional plane Couette flow by various means. At these low Reynolds numbers, there is no doubt that fully resolved direct numerical simulation is feasible and gives accurate results. The purpose of formulating a reduced description is therefore to yield understanding. We now comment on the differences between the approaches used by other authors and our reduction.

In parallel with their experiments, Prigent *et al.* (2002; 2003) considered a pair of coupled Ginzburg–Landau (GL) equations with additive noise as a model for the transition from uniform turbulence to turbulent–laminar banded patterns via noisy (intermittent) patterns. These equations describe the variation in time and spanwise coordinate of the amplitudes $A^{\pm}$ of two sets of laminar bands at opposite tilt angles. These laminar bands modulate the uniform turbulence in competition with one another. Each equation separately has one reflection symmetry which corresponds physically to the centrosymmetry $\kappa_{yz}$ (equation (3.6)) of a banded pattern. The coupled GL equations possess a second reflection symmetry, corresponding physically to a spanwise reflection, which takes the amplitude $A^{+}$ to $A^{-}$ and vice versa. By design, this symmetry is not present in our numerical computations. Prigent *et al.* used their experimental results to fit the parameters in the GL equation and then compared simulations of the equations with experimental results. Steady patterns in the resulting GL equations have only one non-zero amplitude and this amplitude possesses the reflection symmetry corresponding to $\kappa_{yz}$. Hence, the steady patterns in these simulations have exactly the symmetries of the patterns we have considered.

An important class of models aims at reproducing dynamics of streamwise vortices and streaks in plane Couette turbulence by using a small number of ordinary differential equations (ODEs). These equations describe the time-evolution of amplitudes of modes with fixed spatial dependence. Waleffe (1997), guided by the discovery of the self-sustaining process (SSP) in direct numerical simulations (Hamilton *et al.* 1995), derived a system of eight ODEs, whose variables represent amplitudes of the key ingredients of the SSP, namely longitudinal vortices, streaks, and streak waviness. This model was later also studied and extended by Dauchot & Vioujard (2000) and by Moehlis, Faisst & Eckhardt (2004).

Two other Galerkin projection procedures have been used to derive ODE models. The most energetic streamwise-independent modes in a principle orthogonal

composition has been used as a basis for a 13-equation model (Moehlis, Smith & Holmes 2002) exhibiting heteroclinic cycles; when streamwise-dependent modes are added, the resulting 31-equation model (Smith, Moehlis & Holmes 2005) reproduces elements of the SSP cycle. Eckhardt and co-workers (Schmiegel & Eckhardt 1997; Eckhardt & Mersmann 1999) have proposed a Fourier space truncation of the Navier–Stokes equations in all three spatial directions leading to a 19-equation model. They calculated turbulent lifetimes and saddle-node bifurcations giving rise to new steady states in this model.

Manneville and co-workers (Manneville & Locher 2000; Lagha & Manneville 2006) have proposed a drastic Galerkin truncation in the cross-channel direction $y$, retaining one or two trigonometric (for free-slip boundary conditions) or polynomial (for rigid boundary conditions) basis functions, but fully resolving both lateral directions. Simulating the resulting PDEs using a Fourier basis, they have been able to study phenomena such as the statistics of lifetimes of turbulent spots in domains with very large lateral dimensions.

The reduction we have presented differs from the aforementioned studies in several respects. Most importantly, we do not describe any time-dependent behaviour. We consider here neither turbulent–laminar patterns which are themselves dynamic (as in Prigent *et al.*), nor the dynamics of streaks and vortices within the turbulence, nor the transient dynamics of turbulence. Instead we focus on the spatially periodic mean flow of steady turbulent–laminar patterns. While the turbulent portions of patterns are dynamic, containing streaks and streamwise vortices, these are on a fine scale relative to spatial scales of interest here. Our model description follows directly from an analysis of full numerical simulations (not from any *a priori* assumptions, physical or phenomenological), that show that all averaged velocity components and forces, including the Reynolds-stress force, are almost exactly trigonometric or constant in the direction of the pattern wavevector. It follows directly that the steady Reynolds-averaged Navier–Stokes equations can be reduced to six ODEs for cross-channel profiles of the Fourier modes.

One of the more significant aspects of this work is the consideration of the force balance in just the laminar region. This balance is expressed by simple equations either in physical space (equation (3.4)), or in Fourier space (equation (3.27)). These equations are particularly interesting because they do not contain the Reynolds stresses, as these are negligible in the laminar region, and hence their implications can be understood without the need for closure assumptions.

As noted in § 3.1, (3.4) implies that a non-zero tilt angle is necessary to maintain the S-shaped $U$-profile in the laminar region. If the patterns were not tilted, the flow would necessarily be laminar Couette flow in the centre of the laminar regions where the turbulence vanishes. We can also derive implications for the relationship between Reynolds number, tilt angle and wavelength of the patterns from (3.4), which we rewrite as

$$\frac{Re\,\sin\theta}{\lambda} = \frac{(U_0 + U_c)''}{2\pi\, y\, U_s}. \tag{4.1}$$

Except where $y\,U_s \approx 0$, the function on the right-hand side is indeed approximately constant across the channel, between about 2.8 and 3.6. The value of $Re\,\sin\theta/\lambda$ used in our simulations is $350\,\sin(24^\circ)/40 = 3.56$.

We may obtain a qualitative understanding of this constant as follows; see figure 28($a$). Observe that in the centre of the laminar region the functional form of $U = U_0 + U_c$ is like $\sin(\pi y)$. Hence its second $y$-derivative can be approximated by

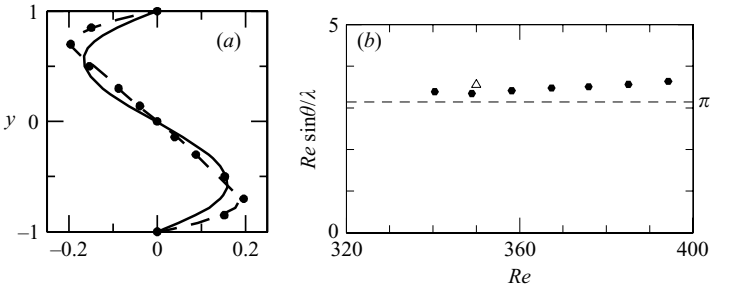


FIGURE 28. (*a*) Comparison of profiles of $U_0 + U_c$ (solid), $(U_0 + U_c)''/(-\pi^2)$ (dashed) and $-2\,y\,U_s$ (points). The profile of $(U_0 + U_c)''/(-\pi^2)$ is close to $U_0 + U_c$, in accordance with the approximate functional form $(U_0 + U_c) \sim \sin(\pi y)$. Note that $(U_0 + U_c)''/(-\pi^2)$ is almost indistinguishable from $-2\,y\,U_s$, showing that $(U_0 + U_c)''/(2\pi\,y\,U_s)$ is near $\pi$ over the entire channel. (*b*) Plot of $Re\,\sin\theta/\lambda$ as a function of $Re$ for the experimentally observed patterns of Prigent *et al.* (2003; 2005). The open triangle shows $Re\,\sin\theta/\lambda = 3.56$ for the case studied numerically in this paper.

multiplication by $-\pi^2$, or equivalently $(U_0 + U_c)''/(-\pi^2) \approx U_0 + U_c$. We also find that the odd function $-2\,y\,U_s$ is close to $U_0 + U_c$ and is in fact almost indistinguishable from $(U_0 + U_c)''/(-\pi^2)$. This implies that the right-hand side of (4.1) is nearly constant across the channel and equal to $\pi$, leading to

$$\frac{Re\,\sin\theta}{\lambda} \approx \pi. \tag{4.2}$$

We believe that (4.2) provides a good first approximation for the relationship between $Re$, $\lambda$, and $\theta$. Figure 28(*b*) shows a plot of $Re\,\sin\theta/\lambda$ as a function of $Re$ from the experimental data of Prigent *et al.* (2003). It can be seen that this combination of quantities is approximately constant with a value near $\pi$. The range of values of the individual factors $Re$, $\theta$, and $\lambda$ can be seen in table 3. In prior studies (Barkley & Tuckerman 2005*a*, *b*), we have studied a large range of Reynolds numbers and tilt angles in a domain of length $L_z = 120$. In this domain, the wavelength of a periodic pattern is less constrained, though it must be a divisor of 120. Figure 29 shows the observed states as a function of $Re$ and $\theta$. Equation (4.2) captures the correct order of magnitude of $Re\,\sin\theta/\lambda$; specifically $1.8 \lesssim Re\,\sin\theta/\lambda \lesssim 5$. Moreover, in figure 29 one sees that for fixed $Re$, $\lambda$ increases with increasing $\theta$, as (4.2) predicts.

Equation (4.2) does not hold in detail, however. Most notably, figure 29 shows that when $Re$ is decreased at fixed $\theta$, the wavelength $\lambda$ increases rather than decreases as one would expect from (4.2). We believe that the force balance (3.4) holds for all patterns which possess a laminar region free of turbulence, but that the additional approximations made in deriving the simple relationship (4.2) do not hold over the full range of conditions considered in figure 29. In particular, the right-hand side of (4.1) depends implicitly on $Re$, $\theta$, and $\lambda$ via the dependence of $U_0$, $U_c$, and $U_s$ on these quantities. The approximate functional relationships between $U_0$, $U_c$ and $U_s$ that we have observed in our simulations and on which we have relied in deriving (4.2) may not hold for other parameter values. Finer adjustments must come from another mechanism.

The main issue not addressed in our study is closure. We have not attempted to relate the forcing of the mean flow due to Reynolds stresses back to the mean flow itself. In the future we will report on studies employing closure models.

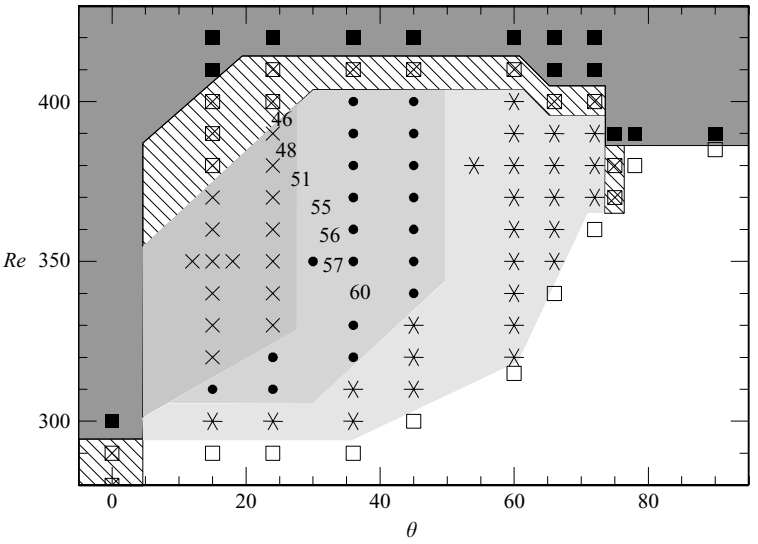


FIGURE 29. Patterns as a function of Reynolds number $Re$ and $\theta$ in a computational domain of size $L_x \times L_y \times L_z = (4/\sin\theta) \times 2 \times 120$. Turbulent–laminar patterns with wavelength $\lambda = 40$ ($\times$), $\lambda = 60$ (●), $\lambda = 120$ ($*$). Uniform turbulence (■), intermittent turbulence (☒), laminar Couette flow (□). Wavelengths in computations are constrained to be divisors of 120. Numbers are wavelengths of experimentally observed patterns of Prigent *et al.* (2003; 2005).

We thank F. Daviaud, O. Dauchot, P. Le Gal, P. Manneville and A. Prigent for helpful comments. The simulations analysed in this work were performed on the IBM Power 4 of the IDRIS-CNRS supercomputing centre as part of project 1119. This work was supported in part by a CNRS-Royal Society grant.

## Appendix. Turbulent–laminar bands in other shear flows

Turbulent–laminar banded patterns have been observed in a number of shear flows: plane Couette (PC) flow, Taylor–Couette (TC) flow, rotor–stator (RS) flow (torsional Couette flow; the flow between differentially rotating disks) and plane Poiseuille (PP) flow (channel flow). Comparisons between these flows are impeded by the fact that different conventions are used to non-dimensionalize each of them.

In order to compare their observations in Taylor–Couette flow with those in plane Couette flow, Prigent *et al.* (2003) generalize the Reynolds number used in plane Couette flow $U = y/h$ by considering it as based on the shear and the half-gap:

$$Re^{PC} = \frac{(\text{shear}^{\text{PC}})\ (\text{half-gap})^2}{\nu} = \frac{(U/h)h^2}{\nu} = \frac{Uh}{\nu}. \tag{A 1}$$

For flows whose shear is not constant, the average shear is used. We also convert streamwise and spanwise wavelengths to total wavelength and angle of the pattern wavevector via

$$\tan(\theta) = \frac{\lambda_{\text{span}}}{\lambda_{\text{stream}}} \qquad \lambda_z = \lambda_{\text{span}} \cos(\theta). \tag{A 2}$$

Table 3 presents the Reynolds numbers, wavelengths, and angles for which turbulent–laminar patterns have been observed experimentally or numerically. The subsections which follow explain how table 3 was obtained from the data in Prigent *et al.* (2003), Cros & Le Gal (2002) and Tsukahara *et al.* (2005).

| | PC | | TC | | RS | | PP |
|---|---|---|---|---|---|---|---|
| $Re$ | 340 | 395 | 340 | 415 | 303 | 438 | 357 |
| $\lambda_{\text{stream}}$ | 110 | 110 | 145 | 95 | 71 | 106 | 103 |
| $\lambda_{\text{span}}$ | 83 | 52 | 70 | 35 | 24 | 36 | 45 |
| $\lambda_z$ | 60 | 46 | 63 | 33 | 23 | 34 | 41 |
| $\theta$ (deg.) | 37 | 25 | 26 | 20 | 19 | 19 | 24 |

TABLE 3. Turbulent–laminar banded patterns in plane Couette (PC), Taylor–Couette (TC), rotor–stator (RS), and plane Poiseuille (PP) flow. Parameters reported in Prigent *et al.* (2003); Cros & Le Gal (2002) and Tsukahara *et al.* (2005) are converted to a uniform Reynolds number based on the average shear and half-gap, as described in the Appendix. The two columns correspond to the values at the minimum and maximum Reynolds number reported.

### A.1. *Taylor–Couette flow*

For Taylor–Couette flow between differentially rotating cylinders, the azimuthal and axial directions correspond to the streamwise and spanwise directions of plane Couette flow. For cylinders of radius $r_i$ and $r_o$, rotating at angular velocities $\omega_i$ and $\omega_o$ with $2h \equiv r_o - r_i$ and $\eta \equiv r_i/r_o$, the shear averaged over the gap is

$$\langle \text{shear}^{\text{TC}} \rangle = \frac{r_i\omega_i - \eta r_o\omega_o}{(1+\eta)h}, \tag{A 3}$$

leading to the Reynolds number

$$Re^{\text{TC}} \equiv \frac{r_i\omega_i - \eta r_o\omega_o}{(1+\eta)h}\,\frac{h^2}{\nu} \approx \frac{Re_i - Re_o}{4\nu}, \tag{A 4}$$

where the last approximate equality corresponds to exact counter-rotation ($\omega_o = -\omega_i$) and the narrow gap limit ($\eta \to 1$), and $R_i$, $R_o$ are the conventionally defined inner and outer Reynolds numbers, e.g. $Re_i \equiv 2hr_i\omega_i/\nu$. The wavelengths and Reynolds numbers observed in Taylor–Couette and plane Couette flow are compared in figure 5 of Prigent *et al.* (2003).

### A.2. *Torsional Couette flow*

The laminar profile for torsional Couette flow between a rotating and a stationary disk (rotor–stator flow) is

$$\boldsymbol{u} = \boldsymbol{e}_\theta\,\frac{\omega\, r\, z}{h}, \tag{A 5}$$

and the Reynolds number based on axial shear and half-gap is

$$Re^{\text{RS}} = \frac{\omega r}{h}\,\frac{h^2}{4\nu} = \frac{\omega r h}{4\nu}. \tag{A 6}$$

For $m$ spirals, the azimuthal wavelength in units of the half-gap is

$$\lambda^{\text{RS}}_{\text{stream}} = \frac{2\pi r}{mh/2} = \frac{4\pi r}{mh}. \tag{A 7}$$

Turbulent spiral patterns which are rather regular occur for a range of angular velocities and radii. In their figures 12, 16 and 18, Cros & Le Gal (2002) focus particularly on the radius and gap:

$$r = 0.8 \times 140\,\text{mm} = 11.2\,\text{cm}, \qquad h = 0.22\,\text{cm}. \tag{A 8}$$

The highest and lowest rotation rates for which turbulent spirals are seen are

$$\omega = 68\,\mathrm{rev\,min^{-1}} = 7.12\,\mathrm{rad\,s^{-1}} \qquad \text{with } m = 6, \tag{A 9a}$$

$$\omega = 47\,\mathrm{rev\,min^{-1}} = 4.92\,\mathrm{rad\,s^{-1}} \qquad \text{with } m = 9. \tag{A 9b}$$

Substituting (A 8)–(A 9) and the viscosity $\nu = 10^{-2}\,\mathrm{cm^2\,s^{-1}}$ of water into (A 6)–(A 7) leads to the values shown in table 3. The pitch angle of the spirals remains approximately constant at 19°. We use (A 2) to calculate $\lambda_{\mathrm{span}}$ and $\lambda_z$, neglecting the variation in radius.

### A.3. *Plane Poiseuille flow*

Figure 14 of Tsukahara *et al.* (2005) shows a visualization from a direct numerical simulation of plane Poiseuille (PP) flow in a channel with domain and Reynolds number

$$L_{\mathrm{stream}} \times L_y \times L_{\mathrm{span}} = 51.2\,\delta \times 2\,\delta \times 22.5\,\delta \qquad Re_c \equiv \frac{u_c \delta}{\nu} = 1430, \tag{A 10}$$

where $u_c$ is the centreline velocity. The domain contains a single wavelength of an oblique turbulent–laminar banded pattern oriented at $\theta = 24°$ to the streamwise direction. (Both the wavelength and the angle are dictated by the computational domain.) Following Waleffe (2003), we view the Poiseuille profile in the half-channel $[-\delta, 0]$, over which the shear has one sign, as comparable to the Couette profile in the channel $[-h, h]$, and thus take $\delta/2$ as the unit of length, rather than $\delta$. The shear is obtained by averaging over $[-\delta, 0]$:

$$\langle \mathrm{shear}^{\mathrm{PP}} \rangle = \left\langle \frac{\mathrm{d}u}{\mathrm{d}y} \right\rangle = \frac{u_c}{\delta}. \tag{A 11}$$

For the Reynolds number based on the average shear and half-gap, we obtain

$$Re^{\mathrm{PP}} = \frac{\langle \mathrm{shear}^{\mathrm{PP}} \rangle\,(\text{half-gap})^2}{\nu} = \frac{(u_c/\delta)(\delta^2/4)}{\nu} = \frac{u_c \delta}{4\nu} = \frac{Re_c}{4\nu} = \frac{1430}{4} = 357.5. \tag{A 12}$$

## REFERENCES


Andereck, C. D., Liu, S. S. & Swinney, H. L. 1986 Flow regimes in a circular Couette system with independently rotating cylinders. *J. Fluid Mech.* **164**, 155–183.

Barkley, D. & Tuckerman, L. S. 2005*a* Computational study of turbulent laminar patterns in Couette flow. *Phys. Rev. Lett.* **94**, 014502.

Barkley, D. & Tuckerman, L. S. 2005*b* Turbulent–laminar patterns in plane Couette flow. In *IUTAM Symposium on Laminar–Turbulent Transition and Finite Amplitude Solutions* (ed. T. Mullin & R. Kerswell), pp. 107–127. Springer.

Bottin, S., Daviaud, F., Manneville, P. & Dauchot, O. 1998 Discontinuous transition to spatiotemporal intermittency in plane Couette flow. *Europhys. Lett.* **43**, 171–176.

Coles, D. 1965 Transition in circular Couette flow. *J. Fluid Mech.* **21**, 385–425.

Coles, D. & Van Atta, C. W. 1966 Progress report on a digital experiment in spiral turbulence. *AIAA J.* **4**, 1969–1971.

Crawford, J. & Knobloch, E. 1991 Symmetry and symmetry-breaking bifurcations in fluid dynamics. *Annu. Rev. Fluid Mech.* **23**, 341–387.

Cros, A. & Le Gal, P. 2002 Spatiotemporal intermittency in the torsional Couette flow between a rotating and a stationary disk. *Phys. Fluids* **14**, 3755–3765.

Dauchot, O. & Vioujard, N. 2000 Phase space analysis of a dynamical model for the subcritical transition to turbulence in plane Couette flow. *Eur. Phys. J.* B **14**, 377–381.

Eckhardt, B. & Mersmann, A. 1999 Transition to turbulence in a shear flow. *Phys. Rev.* E **60**, 509–517.

Hamilton, J. M., Kim, J. & Waleffe, F. 1995 Regeneration mechanisms of near-wall turbulence structures. *J. Fluid Mech.* **287**, 317–348.

Hegseth, J. J., Andereck, C. D., Hayot, F. & Pomeau, Y. 1989 Spiral turbulence and phase dynamics. *Phys. Rev. Lett.* **62**, 257–260.

Henderson, R. D. & Karniadakis, G. E. 1995 Unstructured spectral element methods for simulation of turbulent flows. *J. Comput. Phys.* **122**, 191–217.

Jiménez, J. & Moin, P. 1991 The minimal flow unit in near-wall turbulence. *J. Fluid Mech.* **225**, 213–240.

Lagha, M. & Manneville, P. 2006 On the modeling of transitional plane Couette flow. *Eur. Phys. J.* B, (to appear).

Manneville, P. & Locher, F. 2000 A model for transitional plane Couette flow. *CR Acad. Sci. Paris* II b **328**, 159–164.

Moehlis, J., Faisst, H. & Eckhardt, B. 2004 A low-dimensional model for turbulent shear flows. *New J. Phys.* **6**, 56.

Moehlis, J., Smith, T. & Holmes, P. 2002 Models for turbulent plane Couette flow using the proper orthogonal decomposition. *Phys. Fluids* **14**, 2493–2507.

Pope, S. 2000 *Turbulent Flows*. Cambridge University Press.

Prigent, A. & Dauchot, O. 2000 'Barber pole turbulence' in large aspect ratio Taylor–Couette flow. arXiv:cond-mat/00009241.

Prigent, A. & Dauchot, O. 2005 Transition to versus from turbulence in subcritical Couette flows. In *IUTAM Symposium on Laminar–Turbulent Transition and Finite Amplitude Solutions* (ed. T. Mullin & R. Kerswell), pp. 193–217. Springer.

Prigent, A., Gregoire, G., Chaté, H. & Dauchot, O. 2003 Long-wavelength modulation of turbulent shear flows. *Physica* **D174**, 100–113.

Prigent, A., Gregoire, G., Chaté, H., Dauchot, O. & van Saarloos, W. 2002 Large-scale finite-wavelength modulation within turbulent shear flows. *Phys. Rev. Lett.* **89**, #014501.

Schmiegel, A. & Eckhardt, B. 1997 Fractal stability border in plane Couette flow. *Phys. Rev. Lett.* **79**, 5250.

Smith, T., Moehlis, J. & Holmes, P. 2005 Low-dimensional models for turbulent plane Couette flow in a minimal flow unit. *J. Fluid Mech.* **538**, 71–110.

Tsukahara, T., Seki, Y., Kawamura, H. & Tochio, D. 2005 DNS of turbulent channel flow at very low Reynolds numbers. In *Proc. 4th Intl Symp. on Turbulence and Shear Flow Phenomena*, pp. 935–940.

Van Atta, C. W. 1966 Exploratory measurements in spiral turbulence. *J. Fluid Mech.* **25**, 495–512.

Waleffe, F. 1997 On a self-sustaining process in shear flows. *Phys. Fluids* **9**, 883–900.

Waleffe, F. 2003 Homotopy of exact coherent structures in plane shear flows. *Phys. Fluids* **15**, 1517–1534.